UC Berkeley

UC Berkeley Electronic Theses and Dissertations

Title

Explorations of Space-Charge Limits in Parallel-Plate Diodes and Associated Techniques for Automation

Permalink

Author

Ragan-Kelley, Benjamin

Publication Date

2013

Peer reviewed|Thesis/dissertation

Explorations of Space-Charge Limits in Parallel-Plate Diodes
and Associated Techniques for Automation

by

Benjamin Ragan-Kelley

A dissertation submitted in partial satisfaction of the
requirements for the degree of
Doctor of Philosophy

in

Applied Science and Technology

in the

Graduate Division

of the

University of California, Berkeley

Committee in charge:

Professor Michael Lieberman, Chair
Professor John Verboncoeur
Professor Ka-Ngo Leung

Spring 2013

**Explorations of Space-Charge Limits in Parallel-Plate Diodes
and Associated Techniques for Automation**

Abstract

Explorations of Space-Charge Limits in Parallel-Plate Diodes
and Associated Techniques for Automation

by

Benjamin Ragan-Kelley

Doctor of Philosophy in Applied Science and Technology

University of California, Berkeley

Professor Michael Lieberman, Chair

Space-charge limited flow is a topic of much interest and varied application. We extend existing understanding of space-charge limits by simulations, and develop new tools and techniques for doing these simulations along the way.

The Child-Langmuir limit is a simple analytic solution for space-charge limited current density in a one-dimensional diode. It has been previously extended to two dimensions by numerical calculation in planar geometries. By considering an axisymmetric cylindrical system with axial emission from a circular cathode of finite radius r and outer drift tube $R > r$ and gap length L, we further examine the space charge limit in two dimensions. We simulate a two-dimensional axisymmetric parallel plate diode of various aspect ratios (r/L), and develop a scaling law for the measured two-dimensional space-charge limit (2DSCL) relative to the Child-Langmuir limit as a function of the aspect ratio of the diode. These simulations are done with a large $(100T)$ longitudinal magnetic field to restrict electron motion to 1D, with the two-dimensional particle-in-cell simulation code OOPIC.

We find a scaling law that is a monotonically decreasing function of this aspect ratio, and the one-dimensional result is recovered in the limit as $r >> L$. The result is in good agreement with prior results in planar geometry, where the emission area is proportional to the cathode width. We find a weak contribution from the effects of the drift tube for current at the beam edge, and a strong contribution of high current-density "wings" at the outer-edge of the beam, with a very large relative contribution when the beam is narrow.

Mechanisms for enhancing current beyond the Child-Langmuir limit remain a matter of great importance. We analyze the enhancement effects of upstream ion injection on the transmitted current in a one-dimensional parallel plate diode. Electrons are field-emitted at the cathode, and ions are injected at a controlled current from the anode. An analytic solution is derived for maximizing the electron current throughput in terms of the ion current. This analysis accounts for various energy regimes, from classical to fully relativistic. The analytical result is then confirmed by simulation of the diode in each energy regime.

The simulation approach involved iteratively testing injected ion current, and treating the measured transmitted electron current as a feedback mechanism. The feedback loop was automated, allowing for a single simulation to locate the optimized current. By tuning the injected ion current, we are able to optimize the transmitted electron current. This tuning of the ion current is automated by the integration of a high-level Python interface, wrapping the C++ particle-in-cell simulation code OOPD1. In this particular system, analysis showed that simulation runtime would be a function of transit time, and thus ion mass. By experimenting with reduced ion mass, we were able to significantly reduce simulation times, while recovering the same physical results.

Field-limited emission is an approach for using Gauss's law to to satisfy the space charge limit for emitting current in particle-in-cell simulations. We find that simple field-limited emission models make several assumptions, which introduce small, systematic errors in the system. We make a thorough analysis of each assumption, and ultimately develop and test a new emission scheme that accounts for each. The first correction we make is to allow for a non-zero surface field at the boundary. Since traditional field-emission schemes only aim to balance Gauss's law at the surface, a zero surface field is an assumed condition. But for many systems, this is not appropriate, so the addition of a *target* surface field is made. The next correction is to account for nonzero initial velocity, which, if neglected, results in a systematic underestimation of the current, due to assuming that all emitted charge will be weighted to the boundary, when in fact it will be weighted as a fraction strictly less than unity, depending on the distance across the initial cell the particle travels in its initial fractional timestep. A correction is made to the scheme, to use the actual particle weight to adjust the target emission.

The final analyses involve geometric terms, analyzing the effects of cylindrical coordinates, and taking particular care to analyze the center of a cylindrical beam, as well as the outer edge of the beam, in Cartesian coordinates. We find that balancing Gauss's law at the edge of the beam is not the correct behavior, and that it is important to resolve the profile of the emitted current, in order to avoid systematic errors. A thorough analysis is done of the assumptions made in prior implementations, and corrections are introduced for cylindrical geometry, non-zero injection velocity, and non-zero surface field. Particular care is taken to determine special conditions for the outermost node, where we find that forcing a balance of Gauss's law would be incorrect.

The new emission scheme is tested in a two-dimensional periodic simulation, to demonstrate that the Jaffe limit for a one-dimensional diode with finite initial velocity is recovered. We also extend the iterative scheme developed earlier, and apply it to determine a scaling law for the Child-Langmuir limit in an axisymmetric planar diode, with finite initial velocity. We find that the new scheme reproduces prior results, and in significantly less computation time due to no longer needing to overinject, and leads to rapid convergence of the surface field, using our new algorithmic optimization wrapper to seek the local limiting current along an emitter.

For RCR

Contents

List of Figures

Acknowledgments

First and foremost, I must thank John Verboncoeur, my advisor, for all of his guidance throughout this research process, and our collaborators throughout this work - Ming-Chieh Lin, Yang Feng, and Sang Ki Nam. Pat Berumen, AS&T's administrative hero, for her invaluable assistance. My family - my parents and especially my brother, who has set an extraordinary example to follow. My uncle and late grandfather, who gave me my first job in science and research. And Kira, my fiancée, for her love and support.

Particular thanks to Brian Granger and Fernando Pérez, my mentors in IPython, without whom I would not have had the tools to do this work, and Betty Young, my advisor at Santa Clara who started me on the path of combining physics, engineering, and computer science in my education.

Finally, Jessica Lahey, who continues to remind us to always be students, even after we finally graduate.

Chapter 1

Introduction

Space-charge limited flow is a topic of much interest and varied application. The basic principle of space-charge limits starts with a particular diode system and an applied potential V. As you push more electrons through the gap, the electric-field contributions at the emitting cathode of the electrons already in the gap oppose the field due to the applied potential. Increasing the current through the gap increases the number of particles in the gap, which then further depresses the potential at the emitting cathode, bringing the electric field closer to zero. At some point, the force due to electrons in the gap overcomes the force due to the applied potential. This effect limits the maximum current you can get through a given diode, and there is an analytic solution in the simple case of a one-dimensional infinite planar diode, which is known as Child's law [1].

This has been an area of much research, because the maximum amount of current in a particular geometry has important implications for the design of various devices. Child's law makes many assumptions, so there has also been significant research into systems where those assumptions are not valid, so that researchers can have a good framework for understanding the operating limits of their systems.

Recently, there has been an increase in research into the expansion of Child's law into two and three-dimensional geometries [2] [3]. These expansions have allowed better and more complete understanding of the applicability and scaling of Child's law [4]. Increasingly, in the last twenty years, these expansions have been made via simulations [5]. However, in this relatively short period, tools available to those building simulations have evolved dramatically and rapidly, and some of the simulations tools have failed to take full advantage of technology available [6].

One of the principal advantages of a simulation as opposed to an experiment is greatly improved instrumentation and interaction capabilities. Unfortunately, the tools and languages best suited to sophisticated interaction algorithms are not those best suited for building highly optimized simulations. Fortunately, we now have tools for developing a hybrid application where a high productivity, high-level language can be used for high-level non-performance-critical activities without impacting the performance of the existing optimized code [7]. Since there has been so much good prior work in the simulation codes OOPIC and OOPD1, we should be able to reuse them with minimal disruption, only replacing the user-interface code, allowing much more sophisticated high-level steered simulations.

So our motivation here is to extend our understanding of space-charge-limited current, while developing tools that facilitate such explorations in general. We do this in the hopes that both the specific physical findings and the software tools built in the process will prove useful for future work.

1.1   Child's Law

In 1911, Child and Langmuir derived a simple analytical solution for the maximum current density through a simple diode [1]. Given a simple infinite parallel plate diode, illustrated in Figure 1.1, we can write expressions for the steady state.

The system is described with the simple boundary conditions

$$\Phi(0) = 0 \tag{1.1}$$
$$\Phi(D) = V, \tag{1.2}$$

where Φ is the potential, V is the voltage applied to the diode, and D is the gap separation. In a vacuum, the magnitude of the electric field (E) in this diode is

$$E(z) = -V/D, \tag{1.3}$$

where z is our spatial variable.

In steady state, the magnitude of the current density (J) is uniform in z

$$J(z) = J_{CL}, \tag{1.4}$$

and the Child-Langmuir condition is defined such that the current is limited when the electric field at the cathode is zero,

$$E(0) = 0, \tag{1.5}$$
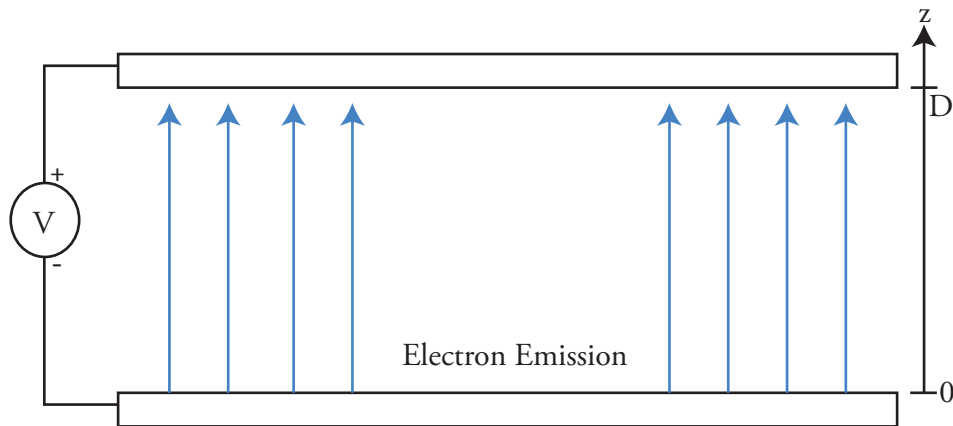
Figure 1.1: A one-dimensional parallel plate diode.

which is to say that the electric field contribution at the cathode from the space-charge already in the gap exactly balances the applied field.

We can write out the expression for energy conservation of electrons,

$$\frac{1}{2}m\left[v(z)\right]^2 - e\Phi(z) = const = 0, \tag{1.6}$$

where m and v are the respective mass and velocity of electrons, and e is the elementary charge. Since this is steady state, the energy is constant throughout the gap, and evaluating at $z = 0$ where both velocity and potential are zero, that constant is zero everywhere. We can also write down Poisson's equation,

$$\nabla^2\Phi(z) = \frac{-\rho(z)}{\epsilon}, \tag{1.7}$$

where ϵ is the permittivity of free space and ρ the charge density. Now, if we rewrite J in terms of ρ and v and note that $J(z)$ is constant in steady state,

$$J(z) = \rho(z)v(z) = -J_{CL}, \tag{1.8}$$

we can combine Equations (1.6, 1.7, 1.8), to get the differential equation,

$$\frac{d^2}{dz^2}\Phi(z) = \frac{J_{CL}}{\epsilon}\sqrt{\frac{m}{2e\Phi(z)}}. \tag{1.9}$$

We can solve Equation (1.9), by rewriting it as

$$\left(\frac{d\Phi}{dz}\right)^2 = \frac{4J_{CL}}{\epsilon}\sqrt{\frac{2m\Phi(z)}{e}} + C \tag{1.10}$$

$$= \frac{4J_{CL}}{\epsilon}\sqrt{\frac{2m\Phi(z)}{e}} + \left(\frac{d\Phi}{dz}\bigg|_{z=0}\right)^2 \tag{1.11}$$

but $d\Phi/dz$ is just $E(z)$, and we have set $E(0) = 0$ in our boundary condition Equation (1.5), so taking the square root of both sides, we get a straightforward differential equation

$$\frac{d\Phi}{dz} = \sqrt{\frac{4J_{CL}}{\epsilon}\sqrt{\frac{2m\Phi(z)}{e}}}, \tag{1.12}$$

in which we can simply combine the Φ terms and integrate

$$\int_{\Phi(0)}^{\Phi(z)} \frac{d\Phi}{\Phi^{1/4}} = \int_0^z \sqrt{\frac{4J_{CL}}{\epsilon}\sqrt{\frac{2m}{e}}}\,dz \tag{1.13}$$

giving us an expression for $\Phi(z)$

$$\Phi(z) = \left(\frac{3z}{2}\right)^{\frac{4}{3}} \left(\frac{J_{CL}}{\epsilon}\right)^{\frac{2}{3}} \left(\frac{m}{2e}\right)^{\frac{1}{3}} \tag{1.14}$$

But since we are actually interested in the limiting current density, we can solve Equation (1.14) at $z = D$, to get

$$J_{CL} = \frac{4\epsilon}{9} \sqrt{\frac{2e}{m}} \frac{V^{\frac{3}{2}}}{D^2} \tag{1.15}$$

which is the maximum steady-state current density through a particular one-dimensional parallel plate diode, known as Child's law.

1.2 Applications of Child's Law

Space-charge effects can have important practical implications for electron beams and diodes, so understanding how various systems are affected has been an important area of research. Investigations have been made into limiting space-charge effects in various environments and situations. One of the more famous of these is the Pierce Gun [8], which uses special cathode geometry to maximize current. Maximizing current is important for device design, and early techniques explored neutralizing space-charge effects by adding positive ions to the system [9]. Space-charge limits were also shown to be significant in cases of cathode fall [10].

Surface effects of space-charge can have significant effects on emission. Fowler and Nordheim found space-charge effects important when exploring the emission of electrons in intense electric fields [11]. There have been a variety of early explorations of the surface effects in emissions under space-charge limited conditions [12] [13] [14].

Space-charge effects can also vary in different environments and materials, which has also been an area of research, exploring space charge effects in semiconductors [15] and solids [16] and insulators [17], as well as specific materials, including carbon nanotube arrays, sharp points, and cones [18] [19] [20] [21] [22]. Space-charge limits can also have strong effects on other processes, such as quantum tunneling [23] and the photoelectric effect [24].

1.3 Extending Child's Law

Child's law is useful as a first estimate of current limits in many situations, but it makes several important assumptions.

- Electrons have zero initial velocity

- There is only one species

- The system is one-dimensional, planar

- The system is in steady-state

There has been much research into relaxing these assumptions over the years. Langmuir made early extensions of the initial velocity by analyzing the effects of thermal velocities on space-charge limits [25] [26]. Jaffé extended the theory to include a uniform initial velocity of electrons [27], which has been further generalized more recently [28] [29].

Non-classical physics has also been added to the Child-Langmuir system. Jory and Trivelpiece extended the energy calculation to include relativistic effects [30], which has been further explored recently [31] [32]. Quantum effects have also been explored [33] [34] [35].

Relaxing the single-species assumption has also been a matter of research, both for experiment and theory. Adding positive ions to the system neutralizes the space-charge effects, which has been explored in various scenarios [36] [37], and incorporating relativistic effects [38].

Where there has been perhaps the most work extending Child's law is in geometry. In the seventies, Wheeler further extended Child's law by adding (still one-dimensional) spherical treatment for concentric spheres [39], which has since been extended to cylinders [40]. More recently, there have been explorations of two-dimensional effects, developing scaling laws for various geometries. Cartesian 2D has been studied [2] [41] [42] [43], as well as axisymmetric 2D [44] [45], and even wedge geometries [46]. Some specific attention has been paid to the development of wings at the edge of a finite beam [47] [48]. There have even been three-dimensional simulations [3].

The last assumption of Child's law - that it is steady-state - has also been explored. The time-dependent nature of space-charge limits in transient situations [49] [50] [4], and instabilities [51] [52] have been studied.

1.4   Simulation Tools

Particle-in-cell simulations are a useful approach to exploring these systems, in part because an experimental approach can be taken [53] [54]. One supposed advantage of a simulation approach over an actual experimental one is that interactions that would involve human interaction (simulated device modification, measurement, etc.) can be automated, and can be highly sophisticated and responsive, well beyond what would be feasible for a human and a device. However, in our experience with the OOPIC simulation code [6], we found the application design prohibited such an approach. This experience motivated the development of a new programmatic interface to PIC simulations. The practical benefit of this is that iterative approaches can be developed that might take days or weeks with human interaction can be run in a fraction of the time (sometimes an order of magnitude) when the formerly human input can be automated.

There are many programming languages and environments, each with their own advantages and disadvantages. Physics simulation codes tend to be written in C/C++ or FORTRAN, which are low-level languages that allow fine-grained optimizations of performance critical elements. While these low-level languages allow developers to be highly efficient from a performance perspective, they are not well suited to efficient high-level interactions, where performance may not be critical. Since we want to be able to write programs that emulate the human interaction component, rapid

prototyping and expressiveness are much more important than performance for this subset of the simulation tasks.

For these high-level activities, such as input specification, or simulation interaction and steering, a similarly high-level language can provide great benefit. Where XOOPIC suffers most is using the obsolete Tk GUI toolkit as the only mode of user interaction with simulations. There was no way for another program to interact with an XOOPIC simulation, and similarly no way to express additional high-level logic around the XOOPIC simulation.

For this situation, it is highly beneficial to use a high-level language that provides an easy transition between high-level user-interaction code and low-level simulation code. Python is such a language, if not because of any inherent properties of the language itself, but because of the tools and community that are already using Python to this effect [55]. There is even precedence for using the Python language in plasma simulations [5].

1.5 Goals

The primary goals of this work are to expand our understanding of space-charge limits, and develop new methods for further explorations of space-charge limited beams, and plasma systems in general. We make our own extensions of Child's law, by exploring the axisymmetric two-dimensional parallel plate diode, and relativistic upstream ion injection in one-dimension. In order to do these explorations, we also develop some new tools for exploring plasma simulations, which should prove useful in general. These tools aim to make investigation into variations of simulations simpler and more convenient, and we make use of them here, to explore in detail field-emission methods, and to relax a variety of assumptions in earlier work.

Chapter 2

Two-Dimensional Axisymmetric Child-Langmuir Scaling Law

This chapter has been previously published in *Physics of Plasmas* as "Two-Dimensional Axisymmetric Child-Langmuir Scaling Law" [44].

2.1   Background

The limits of current through parallel plate diodes has been an area of interest for many years. For over eight decades, we have had Child's law, a full analytic theory for the space charge limited current density between two plates, provided the system is one dimensional and the initial velocity of the carriers is zero [1] [26] [56]:

$$J_{CL} = \frac{4\epsilon}{9}\sqrt{\frac{2e}{m}}\frac{V^{3/2}}{D^2} \tag{2.1}$$

where e is the carrier charge magnitude, m is the carrier mass, V is the potential gap between the electrodes, D is the gap distance, and ϵ is the permittivity of the gap.

Jaffe expanded this theory to account, with some approximations, for monoenergetic initial velocity of the carriers [27]:

$$\frac{J_{1DSCL}}{J_{CL}} = \left(\left(1+\frac{E}{V}\right)^{\frac{1}{2}} + \left(\frac{E}{V}\right)^{\frac{1}{2}}\right)^3 \tag{2.2}$$

where E/V is the ratio of the initial kinetic energy of the carriers to the gap potential. This been further generalized recently [28].

However, the effects of allowing variation of the system in a second or even third dimension has not been explored until recently. The Cartesian two-dimensional space charge limit, 2DSCL, which allows the beam to have a finite width, and variation and motion along that width, has been recently explored via particle-in-cell (PIC) simulation [2], and the characteristics of space charge

limited emission in PIC has also been explored [57]. The Cartesian case has been well explored recently, investigating the current limits and profiles [47] [43]. Luginsland et. al. found a scaling law, showing that the ratio of the 2D space-charge limited current density, J_{2DSCL}, to the 1D limit, J_CL, predicted by Child is inversely proportional to the ratio of the width of the system to the separation of the plates (W/D). As W grows large compared to D, the system begins to approximate the 1D case and the 1D limit is recovered. Radial emission has also been explored analytically for cylindrical and spherical cases [40] [58], as well as wedge geometries [46]. All these different geometries give a different relationship to the classical 1DSCL.

Here, we have explored a different two-dimensional case - a cylindrical axisymmetric system with axial emission, where we still have a parallel plate diode, but rather than having one lateral dimension be finite and the other be infinite, we have a finite radius and assume rotational symmetry around the axis, as shown in Figure 2.1.

We set out to reproduce the Cartesian 2D results in this new geometry, but there are some significant factors that differentiate the two simulations. The Cartesian simulations considered the 2DSCL to be defined as the point where, injecting a uniform current density, *some* carriers begin to turn back. Thus, that paper defines the 2DSCL as the maximum uniform current density where all injected current is transmitted. We, on the other hand, define the 2DSCL as the maximum current that can be transmitted at steady state through the diode, which means that current is space charge limited at all values of r in the beam. Thus, our 2DSCL is higher than that of Luginsland et. al., but should converge to 1D in a similar manner.

A second differentiating factor is the resolution of the potential minimum. In the case of non-zero initial velocity, for current to turn back, a potential minimum has to exist that is some finite distance from the emitting wall. In our case especially, where carriers are being turned back across the entire beam, it is important to resolve that potential minimum. The 2D Cartesian paper does not attempt to resolve this minimum. A result of this requirement is that we must use a much finer mesh, which in PIC simulation precipitates a need for many more computational particles, and as a result our simulations are computationally larger than those we set out to replicate. In order to maintain a reasonable run time while resolving the potential minimum to several cells, we also had to increase the initial velocity of the electrons.

These first two differences are not specific to cylindrical geometry, rather they result from a different approach to the space-charge limit and would remain if we were simply repeating the Cartesian case. There is, however, one significant difference that is geometric, and that is the presence of a drift tube surrounding the beam. In the Cartesian case, a periodic boundary condition was applied in the lateral dimension, such that the simulated system was an array of line beams. In the cylindrical case, we use an equipotential boundary at the outer radius, R, and keep it relatively far from the beam, such that $(R-r)/L$ is always at least 1-20. The image charge in this drift tube could have an effect on the SCL, so this effect is also investigated.

As shown in Figure 2.1, electrons are emitted axially from one side of the cavity towards the other, accelerated by a gap potential V. The outer wall is kept at $V/2$ to keep the background potential of the cavity symmetric. For this simulation, the gap potential $V = 1kV$, and electrons are emitted with a velocity small $(0.01 * V)$ compared to V.
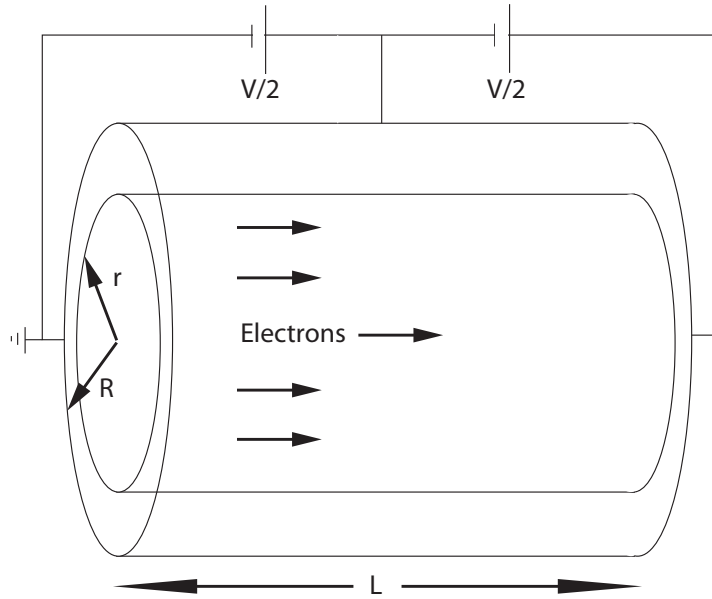
Figure 2.1: The axisymmetric diode

2.2 Numerical Solution

In addition to running PIC simulations, we also solve for the steady state solution with a conventional numerical approach to the Poisson equation in both Cartesian and axisymmetric cases. We will present the scheme and results for Cartesian first, and then the differences for the axisymmetric case. For solution purposes, we assume a very large longitudinal magnetic field, such that $\vec{J}(x,z) = J(x)\hat{z}$. This is an appropriate assumption, because as shown by Luginsland et. al., a large magnetic field makes very little difference in the 2DSCL [2].

Thus, the differential equations to solve are:

$$\nabla^2 \phi(x > x_{beam}, z) = 0 \tag{2.3}$$

$$\nabla^2 \phi(x \le x_{beam}, z) = \frac{J(x)}{\epsilon_o \sqrt{\frac{2e}{m}\phi(x,z)}} \tag{2.4}$$

with the boundary conditions:

$$\phi(x, z = 0) = 0 \tag{2.5}$$

$$\phi(x, z = L) = V \tag{2.6}$$

$$\frac{\partial \phi}{\partial z}(x \leq x_{beam}, z = 0) = E_0 = 0 \tag{2.7}$$

This is not a system that can be solved by simple analytic process due to the nonlinearity in ϕ in the beam, and the fact that J is not specified (it is actually the solution we want). Our scheme involves choosing two initial guesses for J based on the 1D prediction, and then solving the equation for $\phi(x, z)$ without imposing the surface electric field (E_0) boundary condition. Once we have solved for a ϕ, we compare with the E_0 condition, and use Richardson extrapolation to pick a new J, and repeat until ϕ converges to a solution satisfying the E_0 condition [59]. Thus, each iteration of the scheme starts with a previous guess for the current profile: $J(x)$ discretized as J_i, defined along the x-axis.

Inner Iteration: Finite Difference

The inner (ϕ) iteration scheme takes this preliminary J_i and performs a second order finite difference approach to Poisson's equation:

$$\nabla^2 \phi_{i,j} = \frac{\phi_{i+1,j} + \phi_{i-1,j} - 2\phi_{i,j}}{\Delta x^2} + \frac{\phi_{i,j+1} + \phi_{i,j-1} - 2\phi_{i,j}}{\Delta y^2} = -\frac{J}{\epsilon_0 v_{i,j}} \tag{2.8}$$

With this approximation, ϕ is evolved, using the scheme:

$$\phi_{i,j}^{n+1} = \phi_{i,j}^n + \theta \frac{f_{i,j} - \nabla^2 \phi_{i,j}}{D} \tag{2.9}$$

where

$$f \equiv \text{non-linear part of the Poisson equation}$$

$$D \equiv -2(\frac{1}{\Delta x^2} + \frac{1}{\Delta y^2})$$

This scheme is evolved until $\Delta\phi/\phi$ converges within some user specified parameter, $10^{-4} - 10^{-7}$ in our cases.

Outer Iteration: Richardson Extrapolation

Once we have solved for ϕ, we examine the E_0 condition. By looking at the previous two values for J_i (J^1 being the current guess, J^2 being the previous guess) and E_0 from the Poisson solve, we extrapolate for J_i to satisfy the E_0 boundary condition:
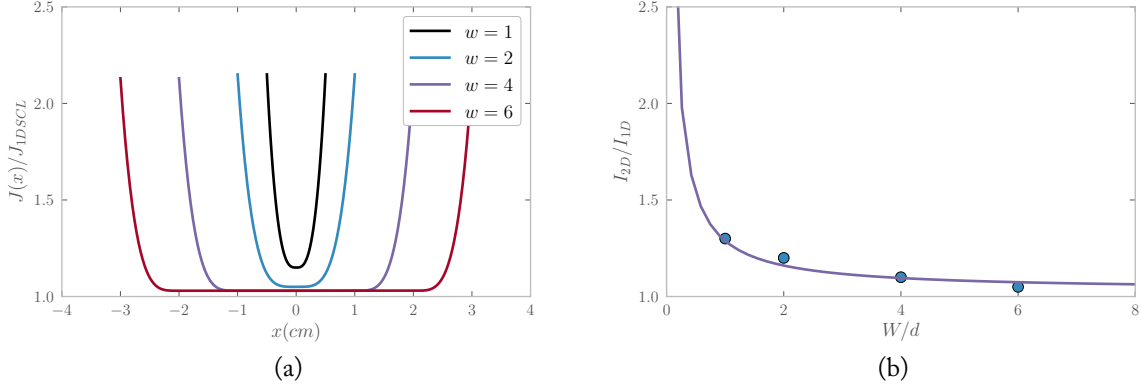
Figure 2.2: Plots of current profile with wings and 2D/1D convergence for the 2D Cartesian case.

$$J^* = -\frac{E_1 + E_2}{2}\left(\frac{J^2 - J^1}{E_2 - E_1}\right) + \left(\frac{J^1 + J^2}{2}\right) \tag{2.10}$$

By weighting our current guess and the extrapolated J^*, we pick a new guess and send that back into the inner iteration to get a new E until the E_0 condition is satisfied within another user specified parameter, $\Delta E_0 / E_0 \leq 10^{-6}$ for our case.

In Figure 2.2, we see 'wings' in the current profile, as previously described [48]. We also recover a scaling law through a curve fit, similar to the Cartesian PIC results:

$$\frac{\bar{J}_{2DSCL}}{J_{1DSCL}} = 1.0307 + \frac{.261}{W/D} - \frac{.0036}{(W/D)^2} \tag{2.11}$$

where

$$\bar{J}_{2DSCL} = \frac{1}{W}\int_{-W/2}^{W/2} J_{2DSCL}(x)dx \tag{2.12}$$

Axisymmetric Case

In the axisymmetric case, the differential equations become:

$$\nabla^2\phi(r,z) = \frac{\partial^2\phi}{\partial z^2} + \frac{1}{r}\frac{\partial}{\partial r}(r^2\frac{\partial\phi}{\partial r}) = 0; \qquad\qquad r > r_b \tag{2.13}$$

$$\nabla^2\phi(r,z) = \frac{J(r)}{\epsilon_o\sqrt{\frac{2e}{m}\phi(r,z)}}; \qquad\qquad r \leq r_b \tag{2.14}$$

with the boundary conditions:
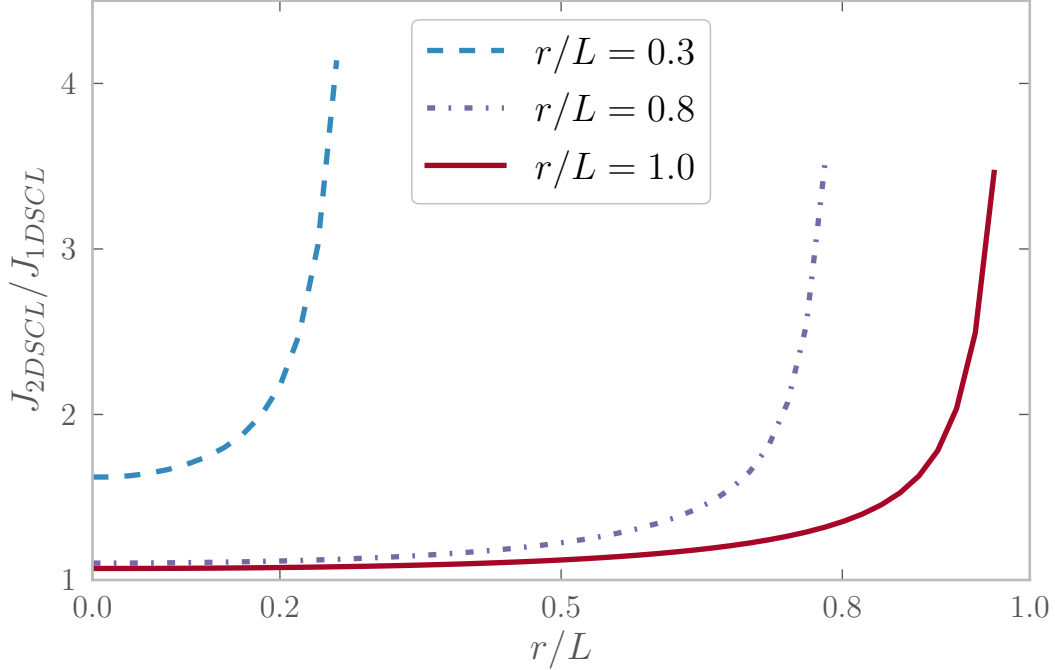
Figure 2.3: Current profile

$$\phi(r, z = 0) = 0 \tag{2.15}$$

$$\phi(r, z = L) = V \tag{2.16}$$

$$\phi(r = R, z) = V/2 \tag{2.17}$$

$$\frac{\partial \phi}{\partial z}(r \le r_b, z = 0) = E_0 = 0 \tag{2.18}$$

Applying the same scheme, very little must change, except for the finite difference approximation of the r, z Laplacian:

$$\nabla^2 \phi_{i,j} = \frac{\phi_{i+1,j} + \phi_{i-1,j} - 2\phi_{i,j}}{\Delta r^2} + \frac{1}{i\Delta r} \frac{\phi_{i+1,j} - \phi_{i-1,j}}{2\Delta r} + \frac{\phi_{i,j+1} + \phi_{i,j-1} - 2\phi_{i,j}}{\Delta z^2} \tag{2.19}$$

As shown in Figure 2.3 the current profile shows that similar wings form in the axisymmetric case, but the larger relative volume of the outer edge in a cylinder allows the wings to have an increased contribution. Again, we recover a scaling law, but the larger contribution of the wings slows the convergence to the 1D limit:

$$\frac{\bar{J}_{2DSCL}}{J_{1DSCL}} = 1.042 + \frac{.231}{r/L} - \frac{.01}{(r/L)^2} \tag{2.20}$$

where

$$\bar{J}_{2DSCL} = \frac{1}{\pi R^2} \int_0^R J_{2DSCL}(r)(2\pi r)dr \tag{2.21}$$

2.3   Simulation

The simulation was done in OOPIC, an electrostatic particle-in-cell code. Just as in the Cartesian case, we used a gap potential of $V = 1kV$, and gap separation of $L = 1cm$. However, our different definition for the SCL required using (r, z) cell dimensions of $(10^{-4}$ m, 2.5×10^{-6} m) with a timestep of 0.125 ps - all much smaller than those used in the Cartesian case. The initial velocity distribution of the electrons was a $10eV$ monoenergetic drift, with an additional thermal distribution of $0.1eV$. The thermal component damps the oscillations that develop in the system [51].

This small initial velocity is just one percent of the gap potential, but Jaffe's formula shows that even one percent produces a significant change in the predicted 1DSCL, versus Child's law. If we plug $E/V = 0.01$ into Jaffe's equation, then we see that

$$\frac{J_{1DSCL}}{J_{CL}} = \left((1.01)^{\frac{1}{2}} + 0.01^{\frac{1}{2}}\right)^3 = 1.105^3 = 1.35 \tag{2.22}$$

So, an initial velocity of one percent of the gap potential results in an increase of thirty-five percent in the 1DSCL analytic prediction.

The procedure we use for determining the 2DSCL is to inject a current that is 2-4 times the 1D prediction, and run the simulation for twenty nanoseconds, which is approximately twenty transit times, measuring the output current and current density profile over the last 1000 timesteps. Overinjecting the current produces oscillations in the system, but the small thermal distribution in initial electron velocity allows the oscillations to damp quickly, to near zero in 3-5 ns.
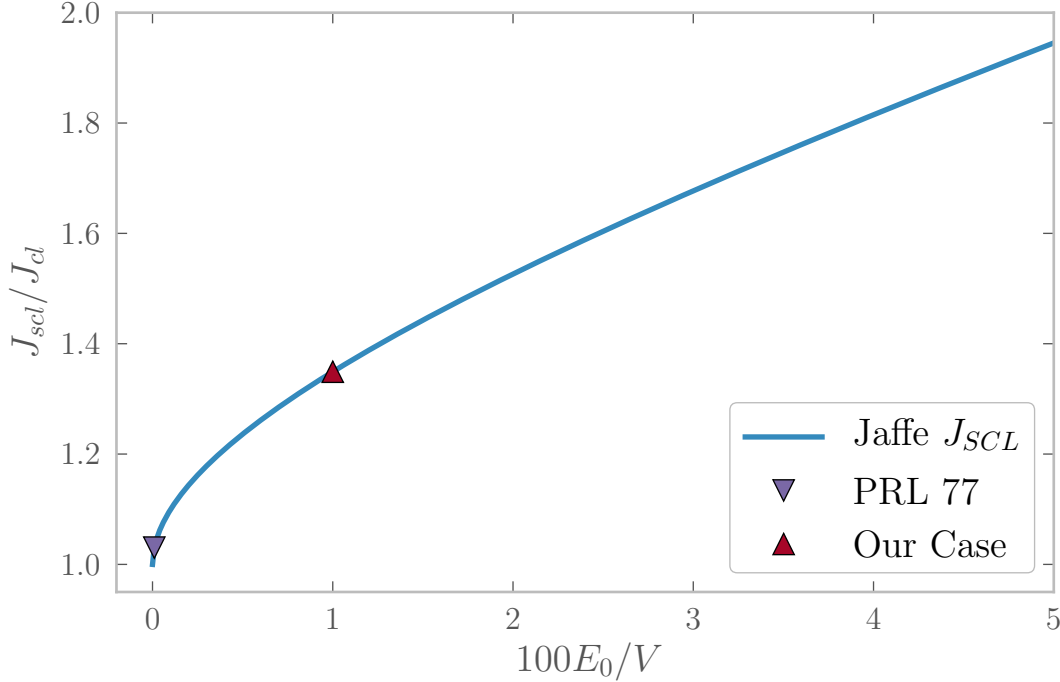
Figure 2.4: Jaffe's scaling law for monoenergetic initial velocity, showing our operating point

2.4 Discussion

To ensure that we reach a steady state, we added a small thermal distribution of initial velocity to damp oscillations. From the temporal evolution of the kinetic energy shown in Figure 2.5, the system is quickly damped in 3-4 oscillations, and since we measure after approximately twenty, we consider asserting steady state to be reasonable.

We do indeed find an axisymmetric scaling law for $\bar{J}_{2DSCL}/J_{1DSCL}$, of the expected form. The larger relative contribution of the wings likely prevents the system from approaching the 1D limit as rapidly as was seen in the Cartesian case:

$$\frac{\bar{J}_{2DSCL}}{J_{1DSCL}} \approx 1 + \frac{.419}{r/L} + \frac{.036}{(r/L)^2} \tag{2.23}$$

As predicted in the numerical solution to the equations, we do see wings in the current density profile. The width of the wing seems to be fixed at approximately 0.05cm, so while the contribution of the wing is larger relative to the Cartesian 2D case, it does eventually become negligible relative to the total transmitted current. We can see this readily by examining a rectangular beam with two wings of thickness ϵ and a cylindrical beam with an external wing of the same thickness. If the cylindrical beam has a radius of r_b and the rectangular beam has a width $2r_b$ centered at $x = 0$, then if they had uniform current density J, then the current would be:
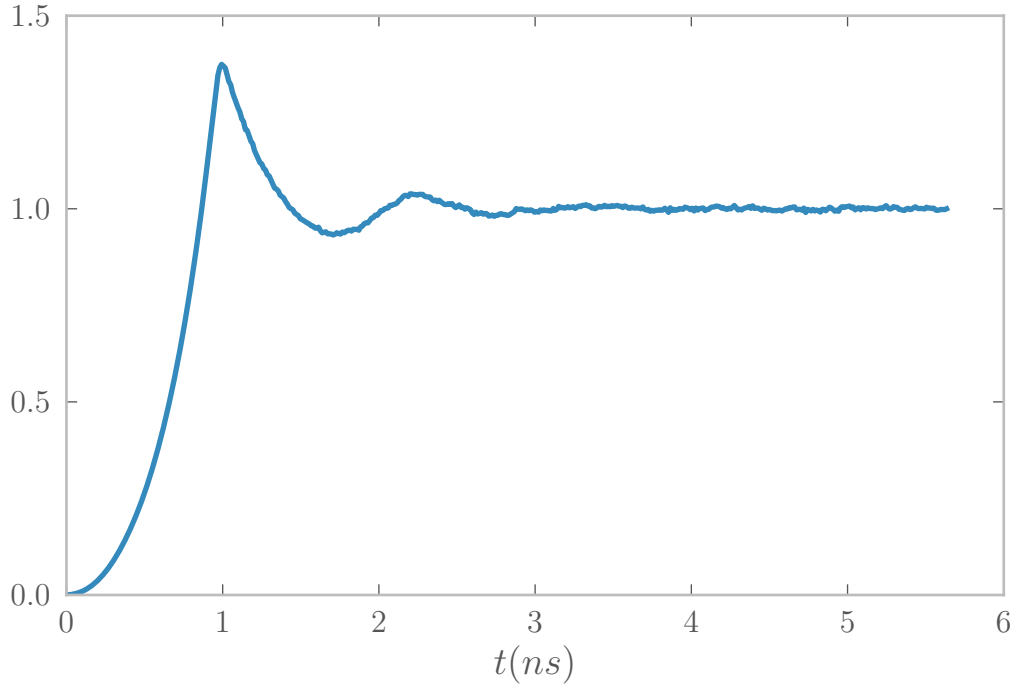
Figure 2.5: Kinetic energy (normalized to final value) of the particles versus time, shows damping oscillations.

$$\text{Cartesian}: \frac{dI_0}{dy} = 2 \int_0^{r_b} J dx \tag{2.24}$$

$$\text{Axisymmetric}: I_0 = 2\pi \int_0^{r_b} J r dr \tag{2.25}$$

But if, as we see here, there are wings of a polynomial form with a peak of $J(r_b) = 2J(0)$, then J becomes

$$J(|x| < r_b - \epsilon) = J_0 \tag{2.26}$$

$$J(|x| \geq r_b - \epsilon) = J_0 \left(1 + \frac{|x| - (r_b - \epsilon)}{\epsilon}\right)^p \tag{2.27}$$

$$J(r < r_b - \epsilon) = J_0 \tag{2.28}$$

$$J(r \geq r_b - \epsilon) = J_0 \left(1 + \frac{r - (r_b - \epsilon)}{\epsilon}\right)^p \tag{2.29}$$

in which case we can quantify the relative contribution of the wings in the Cartesian case:
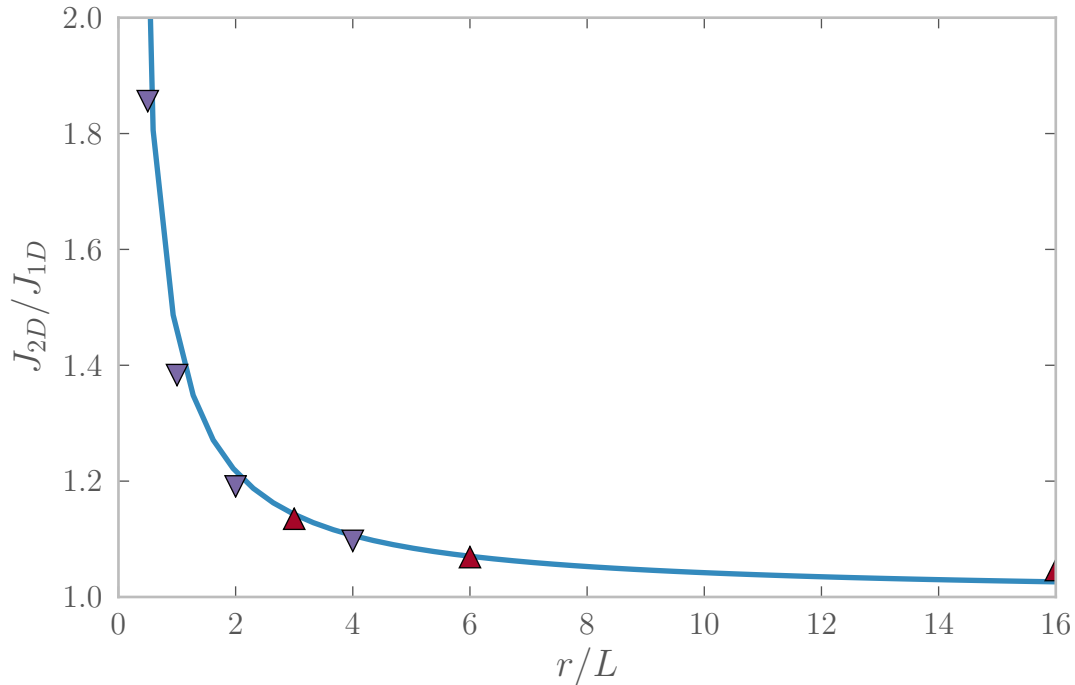
Figure 2.6: The scaling law for the ratio of 2D axisymmetric SCL current to 1D analytic predictions. The convergence to the limit is slow.

$$\frac{I}{I_0} = \frac{\int_0^{r_b-\epsilon} J dx + \int_{r_b-\epsilon}^{r_b} J \left(1 + \frac{x-(r_b-\epsilon)}{\epsilon}\right)^p dx}{\int_0^{r_b} J dx} \tag{2.30}$$

$$= 1 + \frac{1}{r_b} \int_{r_b-\epsilon}^{r_b} \left(\frac{x-(r_b-\epsilon)}{\epsilon}\right)^p dx \tag{2.31}$$

$$= 1 + \frac{1}{r_b} \int_0^{\epsilon} \left(\frac{x}{\epsilon}\right)^p dx \tag{2.32}$$

$$= 1 + \frac{1}{p+1} \frac{\epsilon}{r_b} \tag{2.33}$$

So, as the size of the beam grows relative to the thickness of the wings, the contribution of the wings to the total current decreases with a coefficient of $(p+1)^{-1}$. Repeating the same analysis in the cylindrical case:
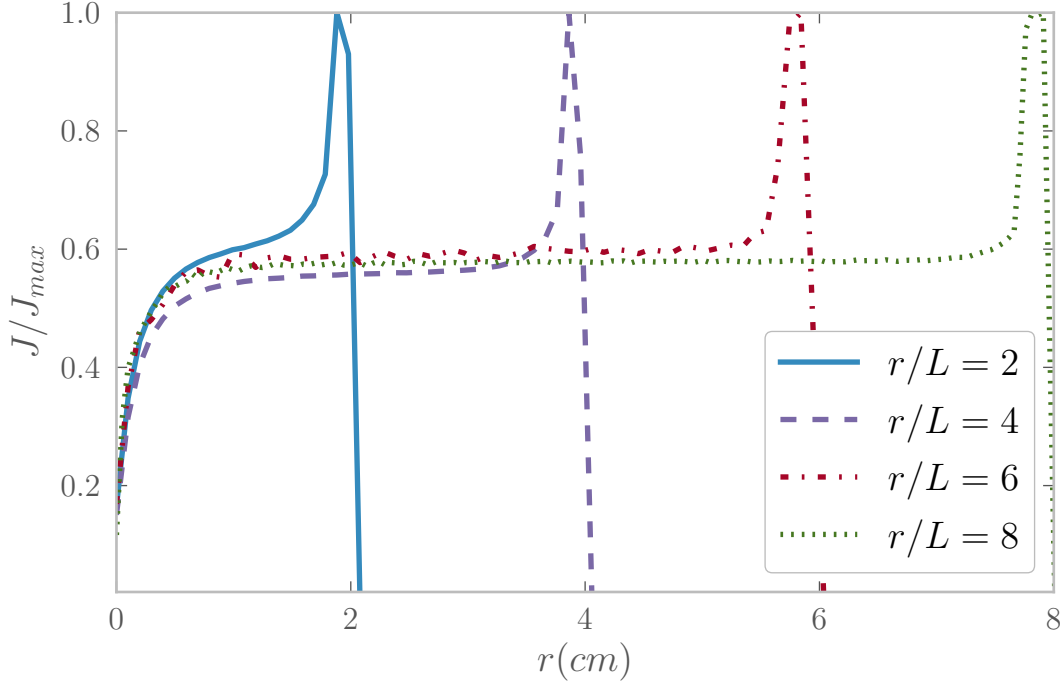
Figure 2.7: Current density profiles from axisymmetric PIC simulations for $r/L = 0.2, 0.4, 0.6, 0.8$ exhibit radial wings.

$$\frac{I}{I_0} = \frac{\int_0^{r_b - \epsilon} Jrdr + \int_{r_b - \epsilon}^{r_b} J\left(1 + \frac{e - (r_b - \epsilon)}{\epsilon}\right)^p rdr}{\int_0^{rbeam} Jrdr} \tag{2.34}$$

$$= 1 + \frac{2}{r_b^2} \int_{r_b - \epsilon}^{r_b} \left(\frac{r - (r_b - \epsilon)}{\epsilon}\right)^p rdr \tag{2.35}$$

$$= 1 + \frac{2\left(2 + p - \frac{\epsilon}{r_b}\right)}{(p+1)(p+2)} \frac{\epsilon}{r_b} \tag{2.36}$$

$$\approx 1 + \frac{2}{p+1} \frac{\epsilon}{r_b}; \left(\text{small } \frac{\epsilon}{r_b}\right) \tag{2.37}$$

So the relative contribution of the wings for larger values or r_b/ϵ in the cylindrical case is approximately twice that of the Cartesian case, but it is still a $1/r_b$ falloff. This explains why we do see slower asymptotic behavior, but still approaching the 1D limit.

The dip in J_{2DSCL} in the center of the beam, measured in the PIC simulations is not predicted by theory. The cause of this dip in not yet clear, but it contributes very little to the total transmitted current, so it does not have a significant effect on the scaling law. The dip is several cells wide,
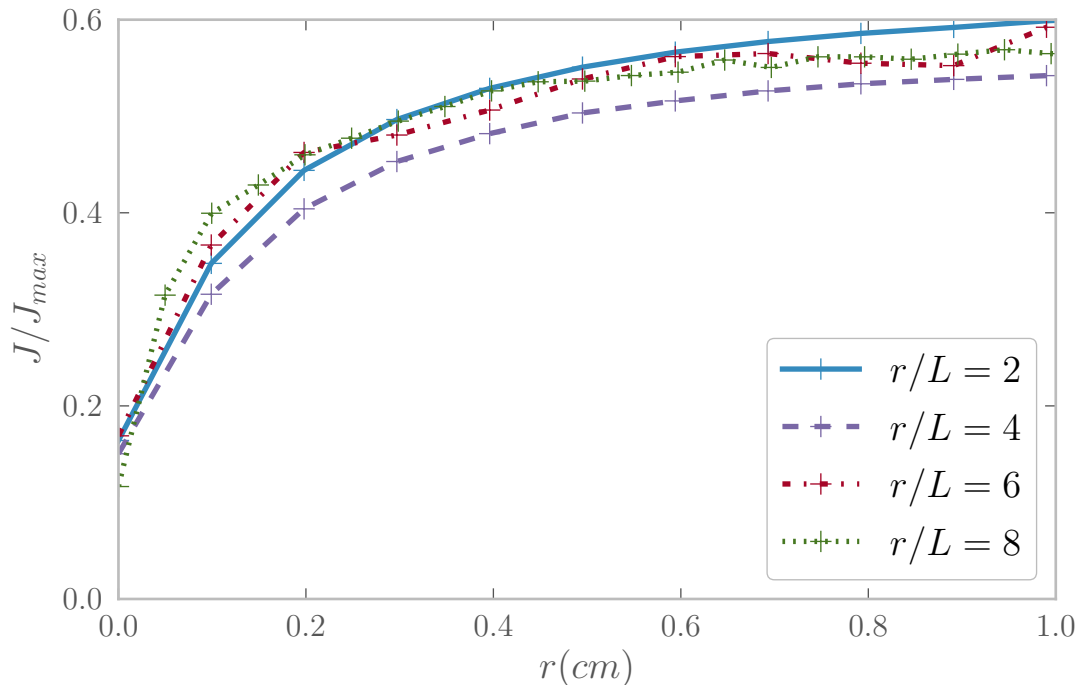
Figure 2.8: Closeup of the current profiles in the center of the beam for $r/L = 0.2, 0.4, 0.6, 0.8$.

and as seen in Figure 2.8, it has a similar shape relative to the peak current density independent of the beam width. Slight beam spreading has been excluded as a possible cause by using an infinite magnetic field particle advance. Statistical effects in the computational model have been eliminated by ensuring that there are many computational particles in the innermost cells of the beam, and using a variable weight emitter, and the dip is not seen when the current density is not space charge limited. None of these changes have provided a significant change in the current density in the center of the beam, and the cause remains a matter of discussion and the object of future work. It remains unclear whether this is a physical result, or the result of numerical effects in the simulation.

Running the simulation for $r = 4L$, but this time varying R between $5L$ and $10L$, keeping the cell dimensions the same, shows that there is a small contribution to the SCL from the drift tube. As we move the wall closer to the beam, we see in Figure 2.9 that the transmitted current increased one to two percent in the range of our simulations. Since we keep the wall location fixed for all our scaling simulations, based on this observation there could be a small relative error, $\Delta J_{2DSCL}/J_{2DSCL}$, of one to three percent as the beam approaches the wall, since it has a small contribution limiting the space charge effects.
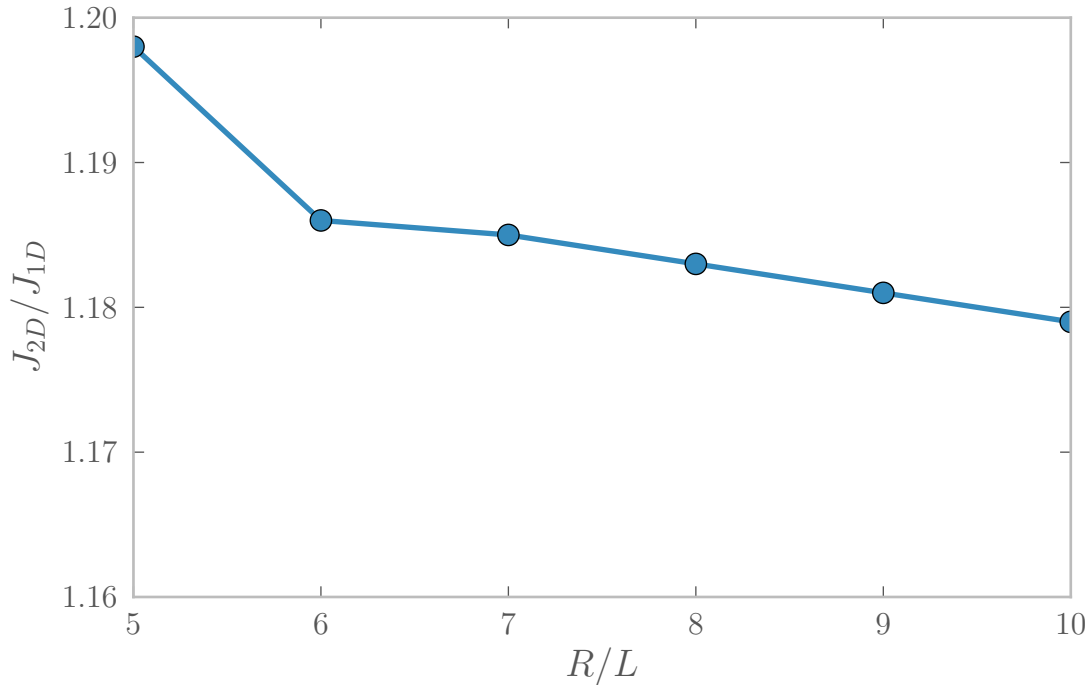
Figure 2.9: Effects of varying the drift tube radius R on the SCL, for $r/L = 4$.

2.5 Conclusions

We have extended prior work in 2DSCL from the Cartesian case to the axisymmetric case with axial emission. A scaling law is found, showing that the maximum space charge limited steady-state current density scales as r/L relative to the 1D analytic predictions. Two-dimensional theoretical models support results found in both the Cartesian and axisymmetric cases, and a geometric analysis of the contribution of the wings is explored as an explanation of the slower convergence of the axisymmetric geometry, as well as the contribution of image charge in the drift tube. Spatial current profiles are found to have peaks, or 'wings', of nearly fixed width at the edges, similar to the Cartesian case. A dip in the current density in the center of the beam is observed in PIC simulations, and its cause remains unknown.

2.6 Future Work

Exploring the cause of the dip in current density in the center of the beam remains a task of interest, especially if its cause is physical. Should it be shown that flat tipped cathodes produce a current density minimum in the center of their beam, it could prove to be useful information. Expanding the scaling law to 3D cases, such as pin array cathodes also remains to be done.

2.7 Acknowledgments

Chapter 3

Optimizing Physical Parameters in 1-D Particle-in-Cell Simulations with Python

The work in this chapter is in collaboration with Ming-Chieh Lin and John Verboncoeur.

3.1 Background

There are many problems in PIC simulations where an iterative approach is taken to optimize physical parameters. When the only available interface to the simulation is a high-level GUI, then a great deal of human interaction is required in the iteration process [44]. This can be highly inefficient when each iteration may take hours or days. Our goal for this work is to develop a programming model where the input and analysis of simulations happen in the same environment (in our case, the Python programming language).

By having the input and analysis exist in the same interface, and that interface being a fully interactive general purpose programming language, we hope to greatly facilitate an automated analysis and feedback-loop-style simulation pattern, where researchers specify an initial simulation, and describe the analysis for determining when to update, change, or halt the simulation, all in the same place and in the same language. Python is just one example of a robust programming language with relatively simple syntax and high portability, which will allow deployment of multi-step algorithms of virtually unlimited complexity in the optimization process, both in terms of analysis and control. Python has been used in other environments to this effect, with great success [5] [55].

Field-emission of electrons in diodes is a matter of much interest, another extension of the basic Child-Langmuir system [1]. By adding ion current emitted from the anode, it has been shown that the field-emitted electron current can be enhanced well beyond that predicted by the familiar three-halves law in classical regimes [37]. Here we will expand that earlier work to relativistic energy regimes, and present a high-level approach for optimizing the emitted current via a new Python interface to low-level simulation code.
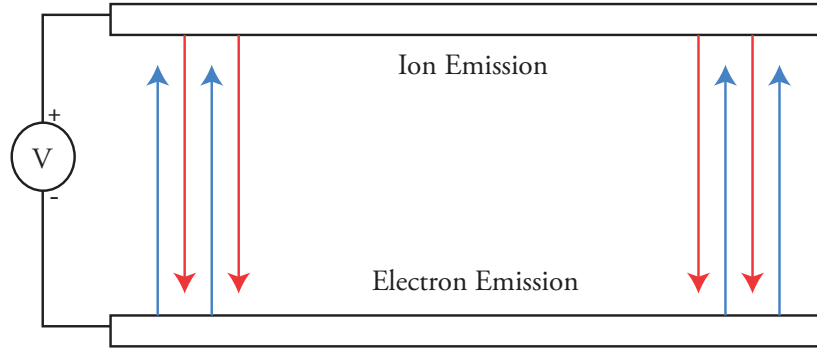
Figure 3.1: The diode system. Ions are injected with fixed current, and electrons via field-emission.

3.2 Model

The System - bipolar flow

The physical system which we explore is that of field-emitted electrons in the presence of ion current in a one-dimensional diode. A fixed current of ions, with ionization level $Z = 1$, is emitted from the anode at a given current density. Electrons are emitted by field emission, governed by the Fowler-Nordheim equation, as expressed in Equation (3.1) [11] [20].

$$J = \frac{AE_s^2}{\phi t(y)^2} \exp\left(\frac{-Bv(y)\phi^{3/2}}{E_s}\right) \tag{3.1}$$

$$t(y)^2 = 1.1 \tag{3.2}$$

$$v(y) = 0.95 - y^2 \tag{3.3}$$

$$y = 3.79 \cdot 10^{-5} \frac{E_s^{1/2}}{\phi} \tag{3.4}$$

where E_s is the surface electric field, ϕ is the work function, and J is our current density.

A fixed DC voltage is applied across the diode, as shown in Figure 3.1.

The transmitted electron current is limited by the space charge in the gap [60]. By adding an upstream ion current, some of the space charge is neutralized, and the maximum transmitted current density is increased. Our goal is to determine the maximum electron current limit for a variety of gap distances and voltages.

We can get a steady-state equation for current in the relativistic bipolar diode, by starting with Poisson's equation and the relativistic conservation of energy [30] [32] [31]:

$$\nabla^2 \Phi = -\frac{\rho}{\epsilon_0} \tag{3.5}$$

$$e\Phi = (\gamma_e - 1)\, m_e c^2 + (\gamma_i - 1)\, m_i c^2 \tag{3.6}$$

where Φ is the potential, ρ is the total charge density, m_e and m_i are their respective masses, e is the magnitude of the electron charge, and γ_e and γ_i are the Lorentz factors for electrons and ions, respectively. Adding the relationship of current to charge density,

$$\rho = \rho_e + \rho_i \tag{3.7}$$

$$J_i = \rho_i v_i \tag{3.8}$$

$$J_e = \rho_e v_e, \tag{3.9}$$

where J_e and J_i are the electron and ion current densities, a solution combining these with Equation (3.1) can be derived [61]:

$$J_e = \frac{\epsilon_0 m_e c^3}{2 e d^2} \left\{ \int_1^{\gamma_{e0}} \left[(\gamma_e^2 - 1)^{1/2} + q\Gamma + \frac{\epsilon_0 e}{2 m_e c J_e} E_s^2 \right]^{-1/2} d\gamma_e \right\}^2 \tag{3.10}$$

$$\Gamma = \left[(\gamma_i + 1)^{1/2} (\gamma_{e0} - \gamma_e)^{1/2} - (\gamma_{i0} + 1)^{1/2} (\gamma_{e0} - 1)^{1/2} \right] \tag{3.11}$$

$$q = (J_i / J_e)(m_i / Z m_e)^{1/2} \tag{3.12}$$

$$\gamma_{i0} = 1 + \frac{Z e V}{m_i c^2} \tag{3.13}$$

$$\gamma_{e0} = 1 + \frac{e V}{m_e c^2} \tag{3.14}$$

where the γ_0 factors correspond to electrons and ions at the full gap potential (V).

Equation (3.12) defines q, a factor describing the ion current relative to the electron current.

We can solve for a steady state of this system in a self-consistent manner by alternating solutions of the Fowler-Nordheim equations with those of Poisson's equation [37]:

We start with an initial guess for J_e, then solve Fowler-Nordheim for E_s. This E_s is plugged into Poisson's equation to find a new value for J_e. This process is repeated until J_e converges within a chosen tolerance, such as .01%:

$$\frac{J_n - J_{n-1}}{J_n} < 10^{-4} \tag{3.15}$$

This iterative process is illustrated in Figure 3.2.

Saturation in various regimes

Now that we have a mechanism for getting solutions for J_e in this system, we can explore various values of q, our ion current parameter. $q = 0$ corresponds to no ion current at all, and increasing q
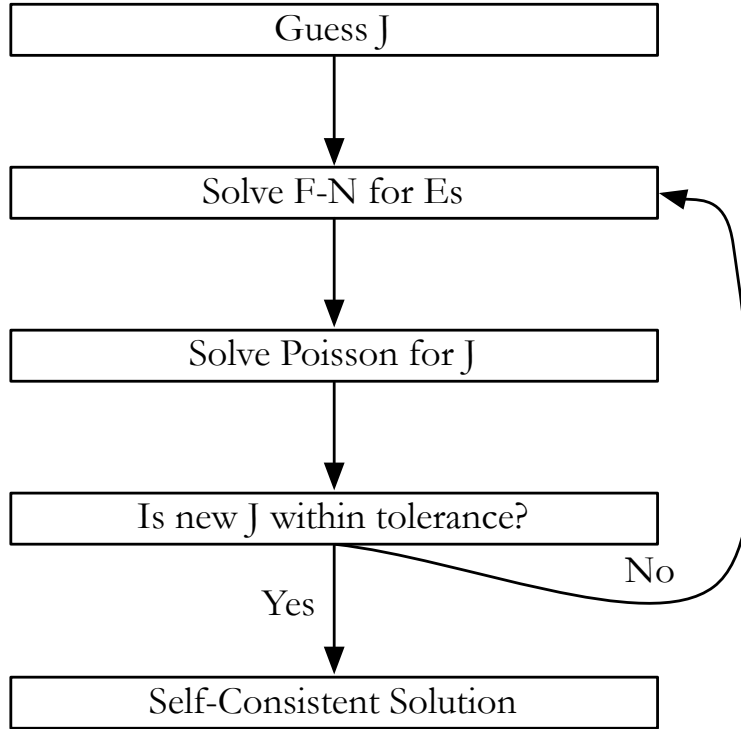
Figure 3.2: Iterative approach to self-consistent solution to steady state of bipolar diode.

means increasing the ion current from the anode. We can define a saturation value (q_s) by setting the surface electric field to zero at the anode in Equation (3.10). This corresponds to space-charge limited emission of ions, and should indicate a maximum steady-state value for both J_i and J_e.

$$q_s = (\gamma_{i0} + 1)^{-1/2}(\gamma_{e0} - 1)^{-1/2}\left[(\gamma_{e0}^2 - 1)^{1/2} + \frac{\epsilon_0 e E_s^2}{2m_e c J_e}\right] \tag{3.16}$$

By expanding Equations (3.13)-(3.14) into Equation (3.16), we get Equation (3.17), a full expression of the saturation factor q_s,

$$q_s = \left(\frac{ZeV}{m_i c^2} + 2\right)^{-1/2}\left(\frac{eV}{m_e c^2}\right)^{-1/2}\left[\left(\left(\frac{eV}{m_e c^2} + 1\right)^2 - 1\right)^{1/2} + \frac{\epsilon_0 e E_s^2}{2m_e c J_e}\right], \tag{3.17}$$

and can proceed to make observations in various energy regimes, where different terms will vanish, depending on eV relative to the rest masses of our electrons and ions.

In the non-relativistic regime, we apply the limits

$$eV << m_i c^2, m_e c^2 \tag{3.18}$$

to Equation (3.17), and get q_{sNR} for the non-relativistic case after plugging in the Fowler-Nordheim solution for J_e:

$$q_{sNR} \approx \frac{1}{\sqrt{2}} \left(\frac{eV}{m_e c^2} \right)^{-1/2} \left[\left(\frac{2eV}{m_e c^2} \right)^{1/2} + \frac{\epsilon_0 e\phi t(y)^2}{2m_e cA \exp\left(\frac{-Bv(y)\phi^{3/2}}{E_s} \right)} \right] \tag{3.19}$$

In the intermediate regime, we have relativistic electrons and non-relativistic ions:

$$m_e c^2 << eV << m_i c^2 \tag{3.20}$$

This gives our simplified q_s as:

$$q_{sR} \approx \frac{1}{\sqrt{2}} \left(\frac{eV}{m_e c^2} \right)^{-1/2} \left[\left(\frac{eV}{m_e c^2} \right) + \frac{\epsilon_0 e\phi t(y)^2}{2m_e cA \exp\left(\frac{-Bv(y)\phi^{3/2}}{E_s} \right)} \right] \tag{3.21}$$

Finally, we have the ultra-relativistic regime (q_{sUR}), where applying the limits

$$m_e c^2, m_i c^2 << eV \tag{3.22}$$

gives us

$$q_{sUR} \approx \left(\frac{ZeV}{m_i c^2} \right)^{-1/2} \left(\frac{eV}{m_e c^2} \right)^{-1/2} \left[\left(\frac{eV}{m_e c^2} \right) + \frac{\epsilon_0 e\phi t(y)^2}{2m_e cA \exp\left(\frac{-Bv(y)\phi^{3/2}}{E_s} \right)} \right] \tag{3.23}$$

Confirming with Simulations

By solving the system with $q = q_s$, we can find the ion current which corresponds to maximum enhancement of the electron current. We can then use this value for J_i as an input to simulations with the PIC simulation code OOPD1 [62].

Running some simulations in each regime shows very good agreement with the theory, as seen in Figure 3.3.
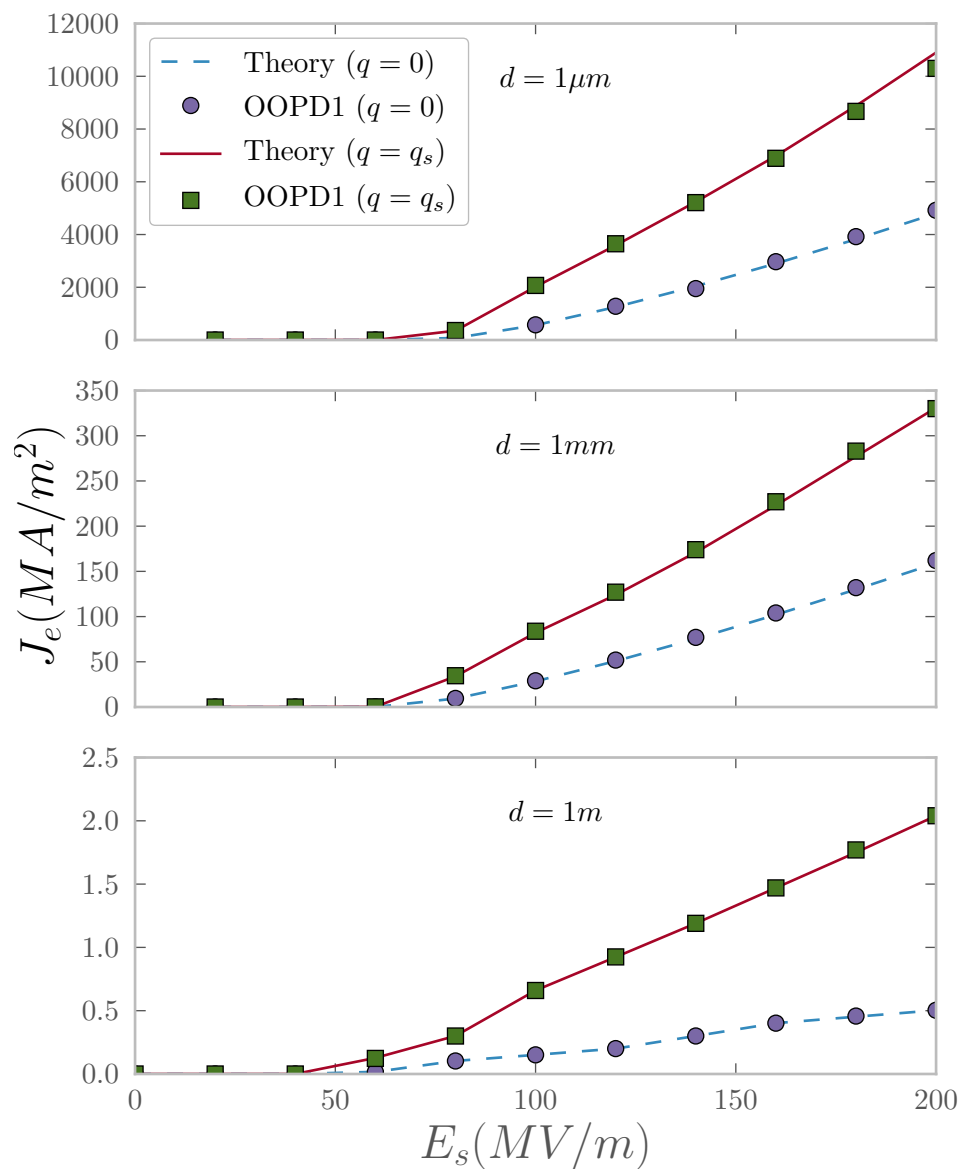
Figure 3.3: Comparison of OOPD1 simulations with theoretical predictions.

3.3   An Alternate Path to q_s

So, we have our solution for q_s, and simulations that confirm the predicted relationship between J_e
and J_i. However, these simulations *do not* actually confirm that this is indeed the maximum value
for J_e and J_i, only that the J_e for a given J_i is correct. If we don't take J_i as given, we can apply an
optimization scheme to find the J_i that maximizes a steady-state J_e. Simulations also allow us to
explore the effects of non-zero initial velocities and temperatures, as well as multidimensional be-
havior, complicated geometry, or other extensions of the model where an analytic solution becomes
intractable.

Optimization Scheme

Recall that our goal is to determine the maximum electron current (J_e) for this diode. The current
limit is a function of the upstream ion current - increasing the ion current allows an increase in
the transmitted electron current by suppressing the space charge effects, but there is a limit to this
enhancement effect. Here we propose an iterative model for determining the minimum ion current
that maximizes the electron output current.

  The procedure we propose is rather simple. For each diode we wish to study, we use the following
steps to determine the maximum current density:

  Setting the initial current and advancing the simulation are fairly clear. The marked steps (with
('-') in the pseudocode, or blue in the flow chart) may require further specification.

  The main purpose of the initial run to steady state is to fill the gap with electrons, and get a
starting value for our measurements. We do this to make sure that no transients related to the initial
traversal of the vacuum are included in our metrics for optimization at future points. This can be a
very loose steady state, where the relative change of the electron current is small:

$$\overline{\frac{dJ_e(t)}{dt}} < f\overline{J_e(t)} \tag{3.24}$$

where the averages are taken over a window δt, (typically a few ion plasma periods ω_{pi}, and less than
one ion transit τ_i). f is a parameter defining a threshold, such as a relative change of $.01\% - 1\%$
over the window.

  Once we have reached an initial steady state we record our initial point (t, J_i, J_e), and can begin
to search for the final value in earnest. Each interaction consists of a linear ramp of the ion current,
which is set in terms of a fixed fraction (r) of the reference current ($J_i(t = 0)$) per τ_i:

$$J_i(t) = J_i(t_0) + \left(\frac{r J_i(t = 0)}{\tau_i} \right) \cdot (t - t_0) \tag{3.25}$$

$$r = 0.2 \tag{3.26}$$

where our initial value for the ramp rate r is 0.2, or 20% of $J_i(t = 0)$ per τ_i.

  The simulation runs with the linearly increasing current until we see evidence of over-injection,
which is the next detail to define. When the space charge limit is exceeded, the system is not stable.

```
       inject an initial ion current density
       advance the simulation
-      while not steady(current):
           advance
-      while not converged:
           ramp ion current linearly
           advance
           if ramp up:
-              while not overinjecting ions:
                   advance
           else (ramp down):
-              while overinjecting ions:
                   advance
-          reverse and reduce the ramp rate
```

(a) pseudocode

(b) decision tree
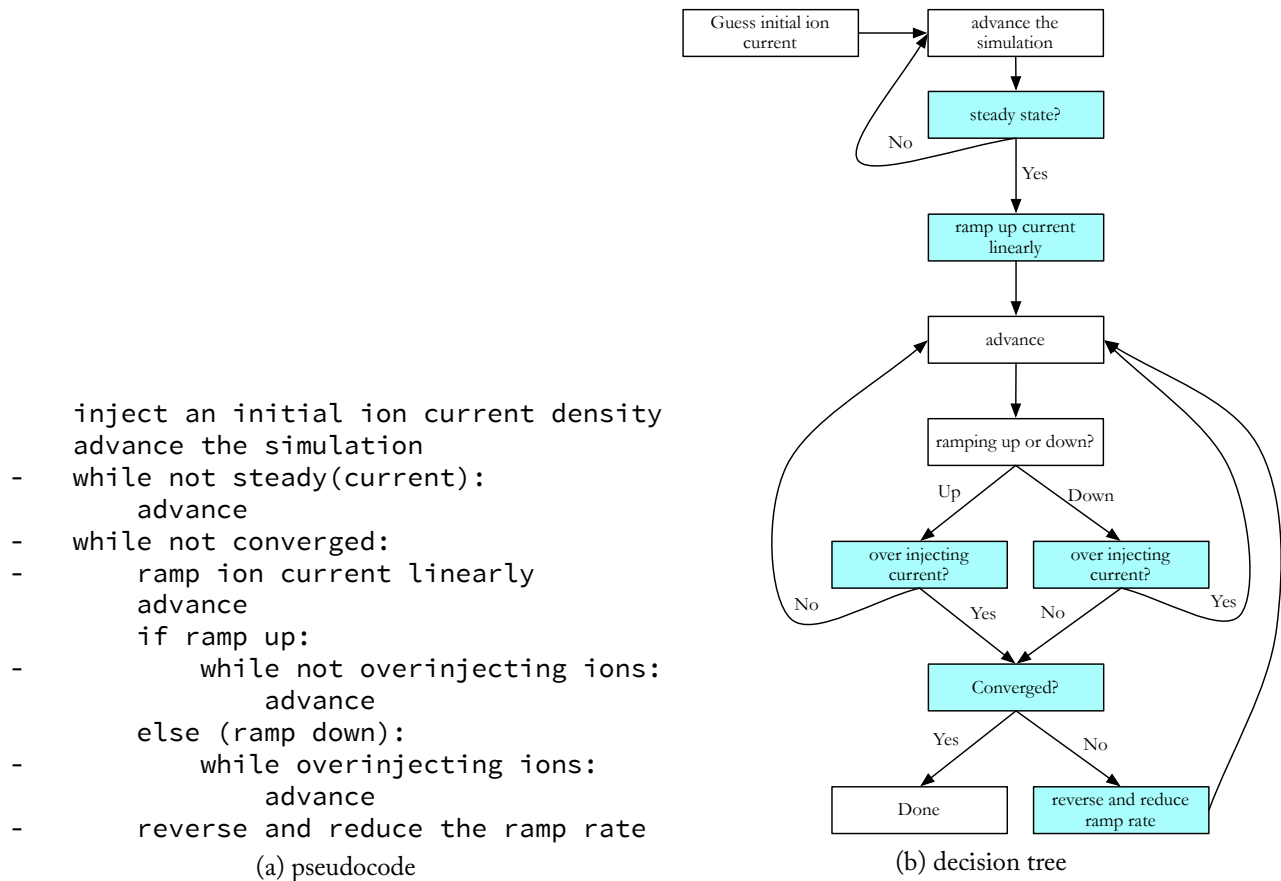
Figure 3.4: The optimization scheme

The excess electrons in the system induce oscillations, which can be observed in the electron output current [51]. Our metric for over-injection is thus defined as when the oscillations exceed some threshold (discrete particle noise will register as small oscillations).

To quantify the oscillations, we look at the recent time history of J_e at the anode. We measure oscillations in the current by looking only at the deviations of the current from a second order regression of it (J_2).

$$dJ(t) = J_e(t) - J_2(t) \tag{3.27}$$

where J_2 is the solution minimizing error Err in the simple linear system:

$$Err = \sum_{j=0}^{k} |J_2[j] - J[j]|^2 \tag{3.28}$$

$$J_2[j] = p_2 t[j] + p_1 t[j] + p_0 \tag{3.29}$$

$$p_2 t[0]^2 + p_1 t[0] + p_0 = J[0] \tag{3.30}$$

$$p_2 t[1]^2 + p_1 t[1] + p_0 = J[1] \tag{3.31}$$

$$...$$

$$p_2 t[k]^2 + p_1 t[k] + p_0 = J[k] \tag{3.32}$$

where k is the number of points in the tail of the current used for the sample, and p_j are the coefficients of the polynomial J_2.

We can now use $dJ(t)/J(t)$ to see the magnitude of oscillations. Once this value exceeds a threshold, we record another point (t, J_i, J_e), and begin to ramp in the opposite direction, at a reduced rate, for example half the previous ramp rate:

$$r_n = -0.5 \cdot r_{n-1} \tag{3.33}$$

Ramping down is the same as ramping up, except that the oscillation threshold is now a lower bound, rather than an upper one. Due to the signal lag of $\tau_e + \tau_i$, we can expect each point we record to be overshot by some fraction. As the ramp rate slows relative to $\tau_i + \tau_e$, that overshoot diminishes, and we converge to a result. We halt the iteration when the difference between upper and lower bound is below a threshold.

3.4 Implementation

In order to implement the scheme described in Section 3.3, we must have access to a few aspects of the simulation. First, we must be able to repeatedly set the ion current at the cathode, and set it to a simple linear function of time. Second, we need access to diagnostic information in order to determine whether the current is steady, and observe oscillations in the output current.

To do this, the existing plasma simulation code OOPD1 was reorganized as a library, and the graphical user-interface replaced with an interface in the Python programming language [62] [63]. By using Python, and particularly the numerical array library numpy, we gain access to a wide variety of data analysis and visualization tools [64]. Using popular, standard, and open data formats means that we no longer need to develop and maintain our own visualization or analysis tools, because so many already exist [65] [66].

There are some caveats to adding the Python layer. The numpy wrapper must be made aware of the layout of the underlying C++ data structures. This does add some potential inconvenience, as some changes to the C++ data layout would necessitate a change in the numpy wrapper code.
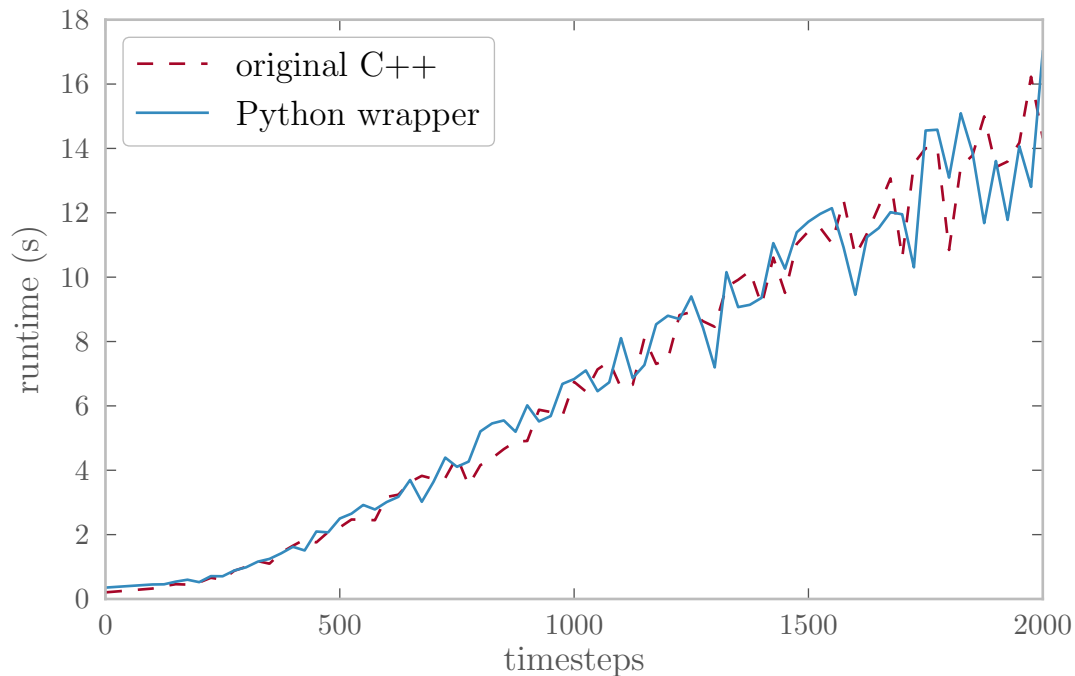
Figure 3.5: Python wrapper incurs no noticeable performance penalty over old C++ OOPD1

Cython and NumPy

When wrapping C++ simulation code in Python, it is important that the overhead of the Python interpreter not be invoked during the inner loop. To minimize the conflict between the high-level interface code and the low-level C++ simulation code, the Cython language is used to expose the C++ OOPD1 objects via the Python C-API [7]. In particular, great care is taken to ensure that diagnostics, which are computed by C++, are never copied, only represented as read-only data via numpy arrays [64]. This minimizes the compute and storage overhead of the Python environment.

Using a sample input file (that will generate results later), and running it for a period of time (Figure 3.5) shows that the performance overhead of wrapping the code in Python does not incur a penalty visible beneath the statistical noise of multiple runs. The slope of the simulation time is initially shallow as the field solve dominates performance. The slope rises linearly as particles enter the gap. Once the gap is full of particles after one transit time (450 timesteps), the slope again becomes linear, as the particle push dominates the field solve, and the number of particles in the system is constant.

Scheme Details

With the programmatic interface, expressing the scheme in Section 3.3 is quite straightforward - We need only express each step in Python code.

The initial setup starts with our initial selection for the ion current (typically the Child-Langmuir current density for ions in a vacuum diode):

$$J_{i0} = J_{CLI} = \frac{4\epsilon_0}{9} \sqrt{2Ze/M_i} \frac{V^{3/2}}{d^2} \tag{3.34}$$

We then run the simulation for at least one ion transit plus one electron transit, and start measuring the electron current at the anode. These transit times (τ_i, τ_e) are approximated by periodically simulating the transit of a test charge across the gap, with classical fourth-order Runge-Kutta (RK4) integration of the particle, while holding the system static:

$$x_0 = L - \epsilon \tag{3.35}$$
$$v_0 = 0 \tag{3.36}$$
$$\dot{x}_n = v_n \tag{3.37}$$
$$\dot{v}_n = \frac{q}{m} E(x_n) \tag{3.38}$$

OOPD1 records the electron current history at the anode (J_e) in its diagnostics, which are made available to Python via Cython and NumPy.

Setting the ramp current is facilitated again by OOPD1, which allows the current to be defined as a simple mathematical expression of time, which is evaluated in C++ at each timestep. We can manipulate this text from Python, allowing us to set the current at the ramp at each turning point. No Python calls are made during the inner loop of the simulation, which is an important performance consideration.

Measuring oscillations uses the same current history diagnostic as the steady-state metric. We start by:

1. taking the most recent data points of the electron current at the cathode

$$J_e = J_e(t > t' - \tau) \tag{3.39}$$

where τ is the sample window of time, and t' is the current time of the simulation.

2. subtracting a second order polynomial regression (provided by NumPy):

```
p = np.polyfit(t,J,2)
Jvar = J - np.polyval(p, t)
```

where `np.polyfit` implements the second-order regression described in Equations (3.28)-(3.32).

Finally 3. applying a simple smoothing-window to suppress particle noise:

```
sJ = smooth(Jvar)
```

where each element in `sJ` is the average of the surrounding $k + 1$ points in `Jvar`:

$$\texttt{sJ}[i] = \frac{1}{k+1} \sum_{j=i-k/2}^{i+k/2} \texttt{Jvar}[j] \tag{3.40}$$

Now we have a quantification of the deviation from a smooth electron current, which we use to measure whether there are oscillations in the current due to over-saturation. This completed, we proceed with convergence as described in Figure 3.3.

3.5   Results

Our simulation results agree quite well with the theoretical predictions in 3.2, from the classical to the ultra-relativistic regime (Figure 3.6).
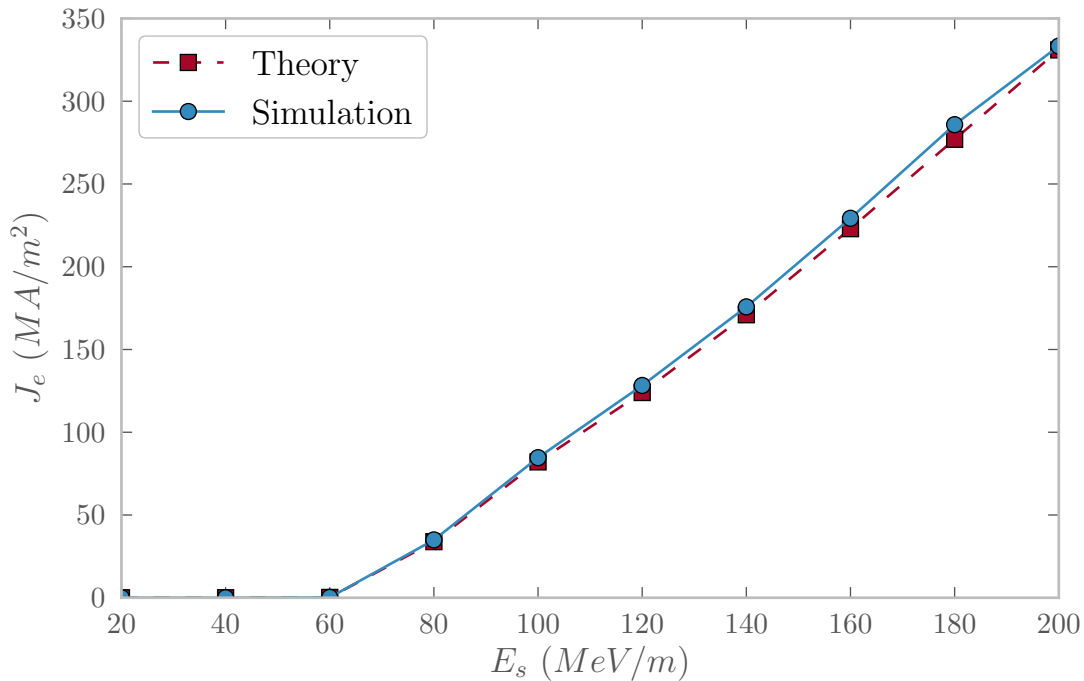
Figure 3.6: Comparison of analytical solution and simulation results

By collecting the input/steering interface and the analysis into the same environment, we have provided a powerful mechanism to express analysis-based simulation evolution. This mechanism allows much more efficient deployment of whole simulation procedures, and fine-grained interaction not convenient or sometimes even feasible via human interaction. With a single programmatic

expression of the simulation *and analysis*, it is straightforward to change the analysis approach, or apply similar analysis to different systems, with minimal difficulty.

Overestimation
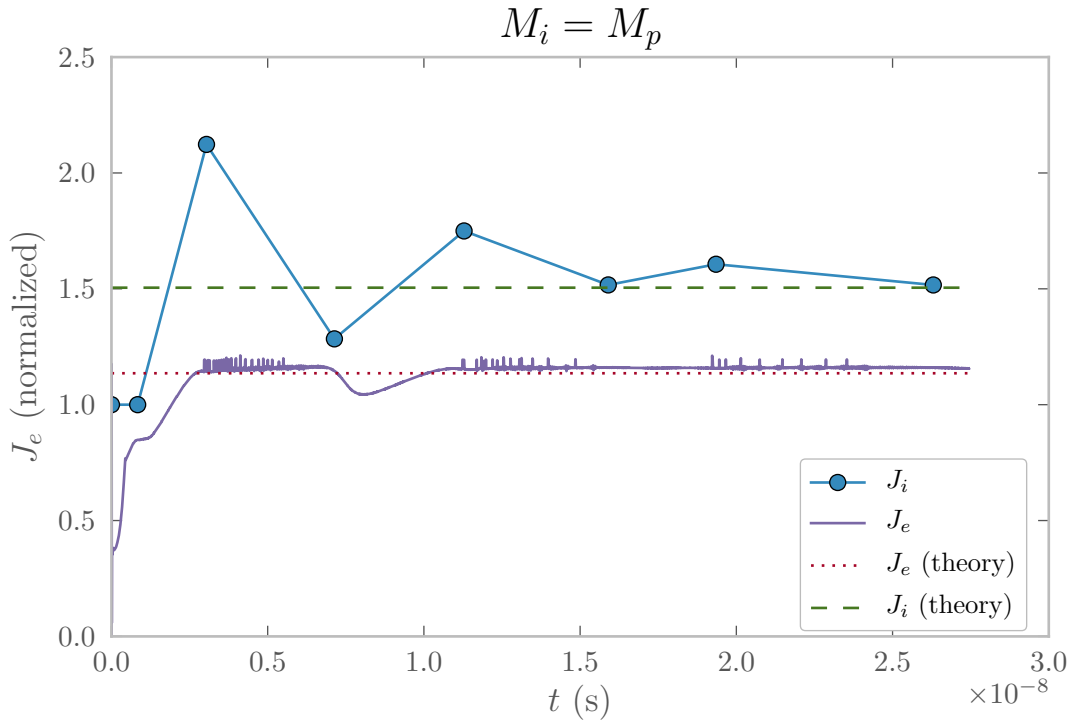
Figure 3.7: A single convergence run for protons

While our measurements agree well with theory, there is a systematic overestimation by approximately two percent (Figure 3.8).

One potential source of this difference is that the theoretical calculation assumes zero initial electron and ion velocities, but the simulation uses room temperature (1/40 eV). However, calculations of nonzero initial velocities would suggest an excess of 0.1-0.2%, not 1-2%, so it is insufficient [26].

Another potential source for the overestimation is the threshold for determining the absence of oscillations, which sets our lower bounds during iteration. Since there is always some small oscillation, this lower threshold cannot be zero. It is possible that the finite lower bound is masking the small initial oscillations introduced by minor overinjection. Increasing the number of simulated particles (reducing the number of simulated particles per physical particle) has no significant effect on this threshold, so the effect does not appear to be due to finite particle noise.

To ensure that we are fully resolving the physics of the system, we can look at some diagnostics. We will look particularly at our $d = 1mm$, $E = 200MeV/m$ system.
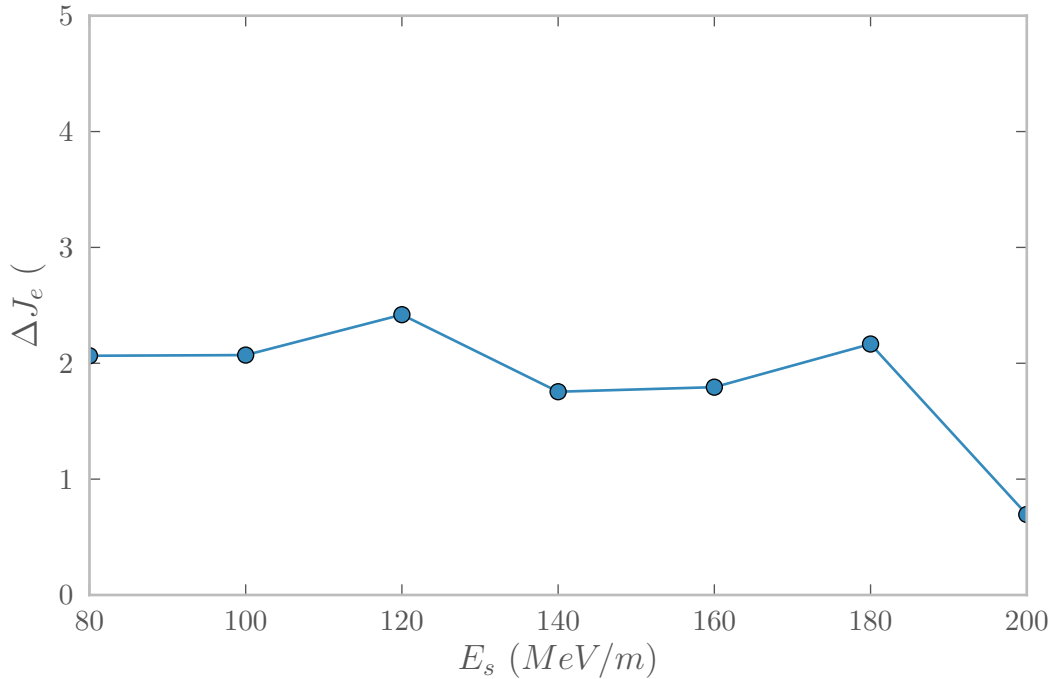
Figure 3.8: Relative error (in percent) of simulation results.

Looking at the number density for ions and electrons, we see that throughout most of the gap, the ion current does indeed neutralize the electron space charge effects. Only very close to either wall do we see any significant space charge effects (Figure 3.9).

We can also look at the phase space of each species, which shows straightforward acceleration across the gap in either direction.

Combining the data in Figures 3.9 and 3.10, we can inspect the Debye length λ_{De}

$$\lambda_{De} = \sqrt{\frac{\epsilon_0 k_B / e^2}{n_e/T_e + n_i/T_i}}, \tag{3.41}$$

and compare it to our grid resolution (Δx), to verify that we are resolving the Debye length everywhere. Figure 3.11 shows the Debye length throughout the diode relative to the grid resolution, demonstrating that it is indeed resolved.
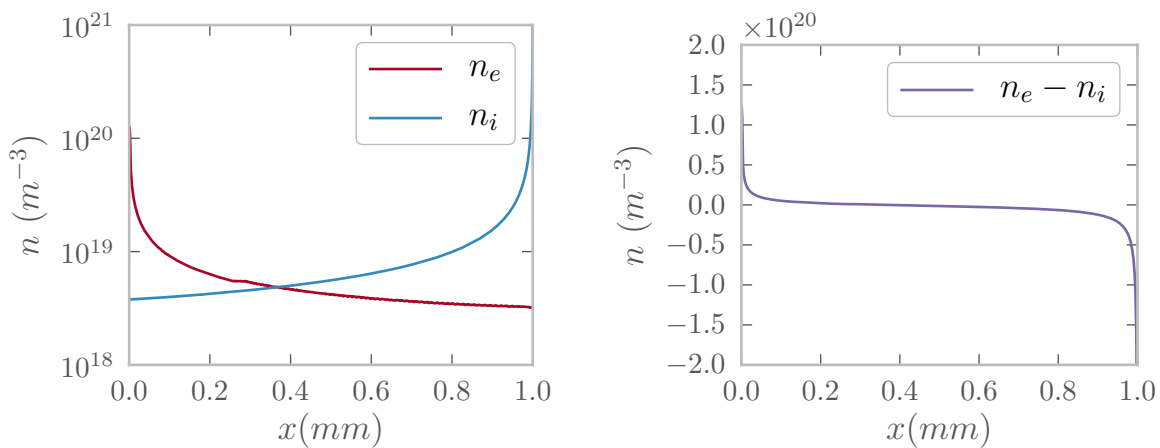
(a) Ion and electron density

(b) Total Density

Figure 3.9: Density for ions and electrons, as well as their difference.
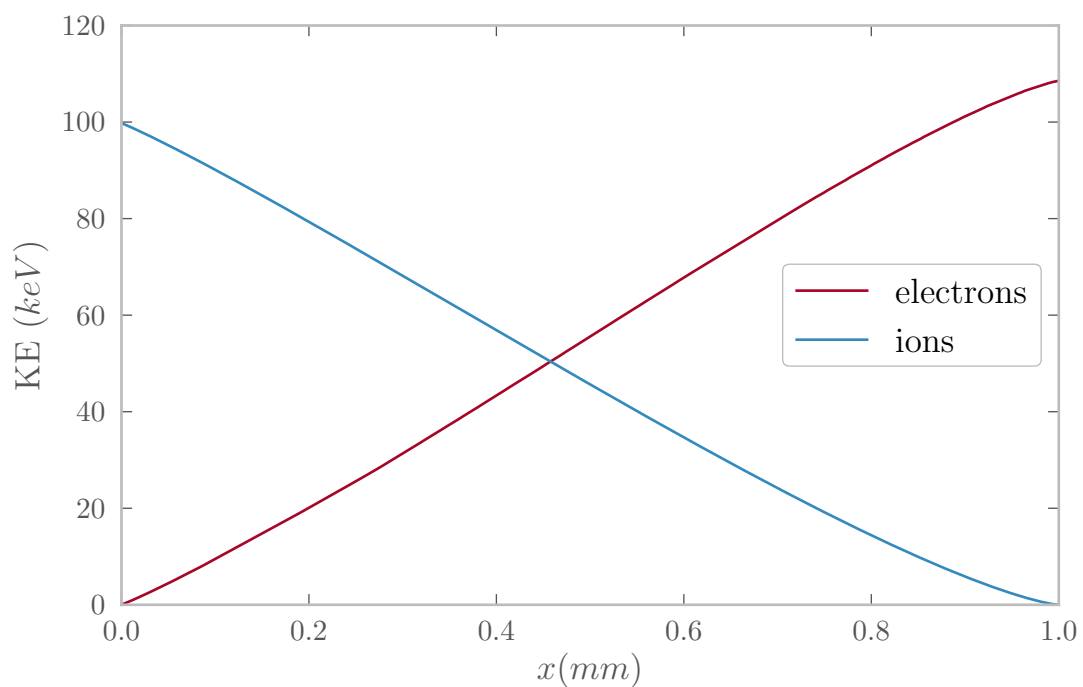
Figure 3.10: Phase space for ions and electrons
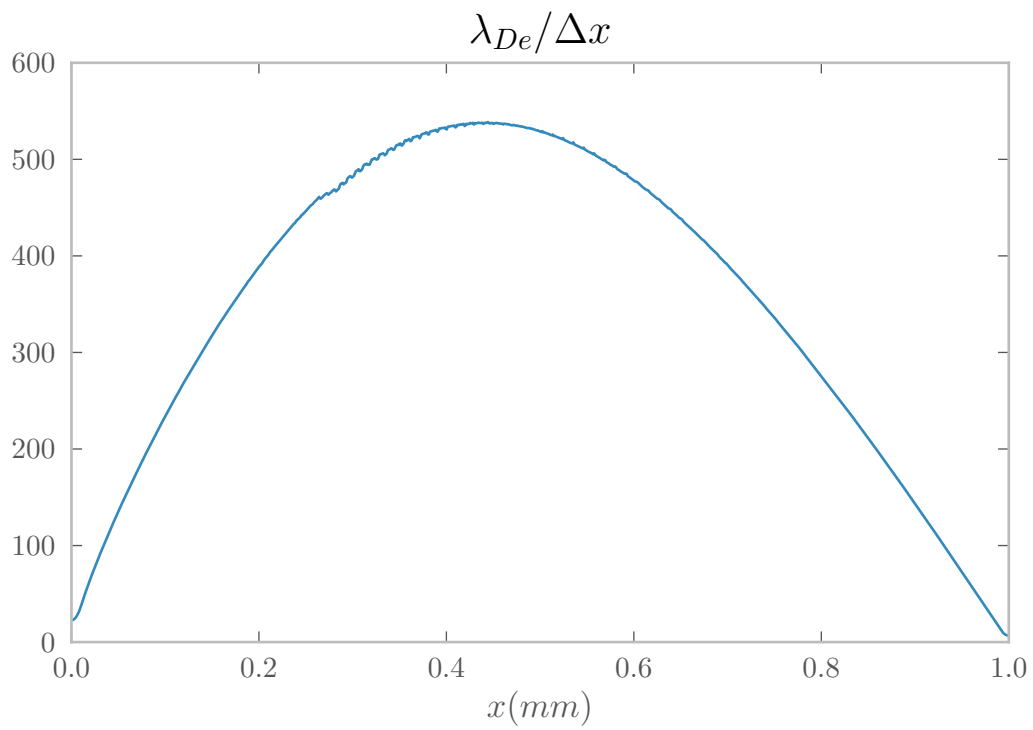
Figure 3.11: Debye length throughout the diode relative to the grid resolution. Clearly, it is well resolved.

Mass Scaling

The convergence time (in both real runtime terms and physical simulation time) is strongly dependent on the mass of ions (M_i). The time it takes for signal from a change in the ion injection current to be measured in the electron output current (both at the anode) scales with the ion transit time (τ_i) plus the electron transit time (τ_e). Making the steady state approximation that fields are constant over this interval:

$$\tau_i \propto \sqrt{\frac{M_i}{ZeV}} \tag{3.42}$$

$$\tau_e \propto \sqrt{\frac{m_e}{eV}} \tag{3.43}$$

So the total transit time is $\tau_i + \tau_e = (1 + \sqrt{\frac{m_e}{M_i}})\tau_i$, which in the case of protons where $M_i >> m_e$ gives

$$\tau_i + \tau_e \approx \tau_i \tag{3.44}$$
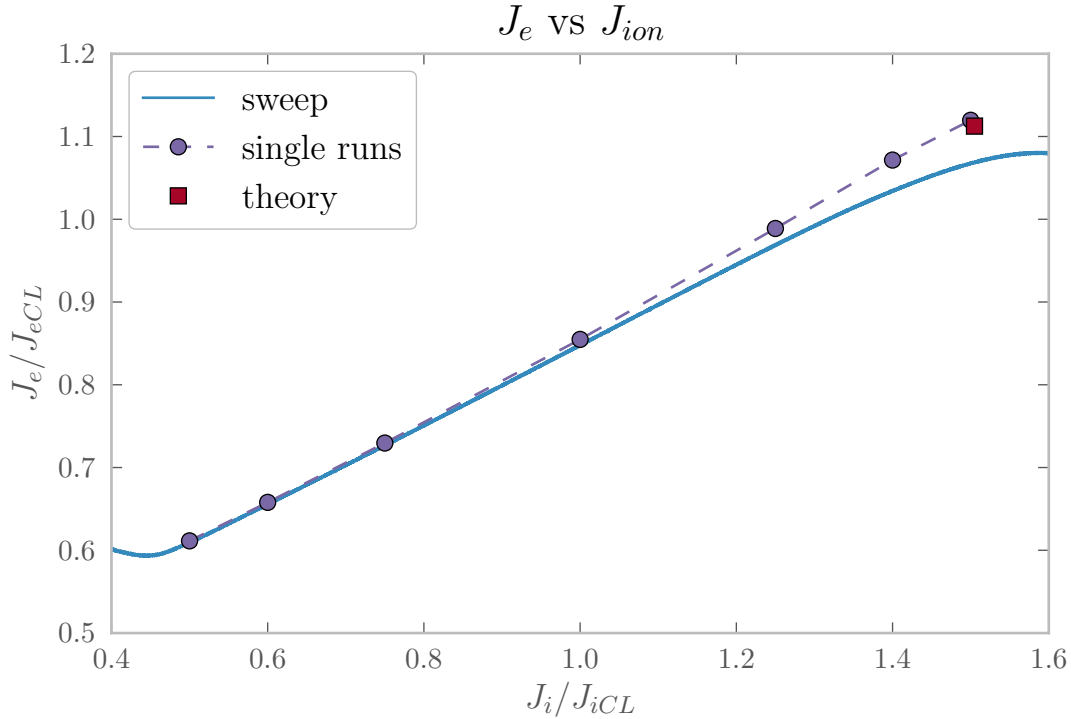
Figure 3.12: Comparison of sweep samples and single-run values

Figure 3.12 shows the lag effect of the transit time by plotting the electron current at time t versus the ion current at $t - (\tau_i + \tau_e)$.

Reducing the ion mass reduces the signal propagation time, which proportionately affects the number of timesteps required for each iteration in the convergence. Reducing the mass by a factor of 100 should reduce the simulation runtime by a factor of 10. The Child-Langmuir current density also scales with $\sqrt{M_i}$. Since the current density and transit time scale inversely with the same factor, the total number of ions in the gap is actually unchanged.

When the ion mass is small enough, then the approximation in Equation 3.44 is no longer valid, and the electron transit time contributes to the feedback time and thus the simulation time.
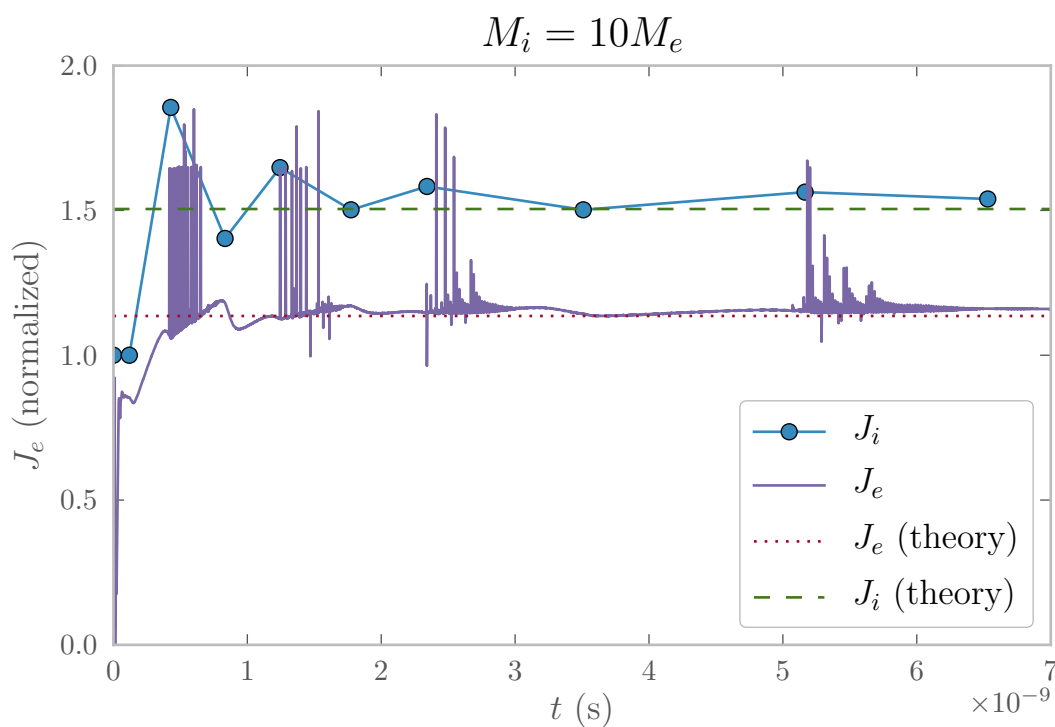
Figure 3.13: Same simulation procedure with $M_i = 10m_e$

Figure 3.13 shows that changing the ion mass ultimately has no effect on the resulting electron current, effectively saving significant time in the simulation. The oscillations can clearly be seen as much larger, and measuring the amplitude of those oscillations shows that it, too, scales with $\sqrt{M_i}$.

To summarize the scalings by the ion mass:

$$\tau_i \propto \sqrt{M_i} \tag{3.45}$$

$$J_{SCL} \propto \frac{1}{\sqrt{M_i}} \tag{3.46}$$

$$A_{oscillations} \propto \frac{1}{\sqrt{M_i}} \tag{3.47}$$

$$N_{ions} \propto J_i \cdot \tau_i \propto 1 \tag{3.48}$$

$$t_{sim} \propto \tau_i \propto \sqrt{M_i} \tag{3.49}$$

all of which are readily observed in the simulations. Ultimately, the same simulation with protons, redone with $M_i = 10m_e$, converged to the same result for J_e and J_i/J_{iCL} (within 0.1%) in less than one third of the time. The only source of difficulty here was the increase in amplitude of the current oscillations, which required adjustments to the oscillation detection thresholds.

3.6 Conclusions

We have shown an analytical solution for maximizing the space-charge limited current through a diode with an upstream ion current, and confirmed this result with two different simulation approaches. The feedback scheme should prove quite useful for systematically exploring different physical systems, particularly where theoretical results are untenable. In exploring the reduced-mass model of the same system, we found an efficient way to explore simulations where transit time is a limiting factor, and are interested in further exploring the applicability of this model. A theoretical analysis of the system suggested that we would see a scaling law, where the runtime of the simulation would be proportional to $\sqrt{M_i}$, and experiments with changing M_i confirm this analysis.

Future Work

This work reveals a few avenues of future study. We explored just one iterative approach to optimizing a physical parameter, but the tools developed here could be applied to numerous other approaches, which could be explored in comparison to the one presented here, or for new physical systems entirely. Of particular interest is exploring in detail the upper and lower bound metrics, which are the weakest part of this scheme, and should be better understood.

It would also be interesting to explore in further detail the implications of the reduced mass model, which may allow more efficient modeling of systems where transit time is a dominant factor in simulation time. The oscillations induced by the parameter change are problematic, because they prolong the simulation time, so it would be valuable to investigate approaches to damping those oscillations. We could also apply this general tool for optimizing a physical parameter to other optimization schemes, which should facilitate the comparison among schemes.

Chapter 4

Relaxing Assumptions in Field-Limited Emission, and an Iterative Approach to the Axisymmetric Scaling Law

Here, we set out to further explore the system described in Chapter 2, with an automated iterative approach developed in Chapter 3.

4.1 Background

We have developed a scaling law for the Child-Langmuir space-charge limited current density in axisymmetric geometry [44]. The previous approach leaves much to be desired. It was known from previous work [48] that the current profile would have peaks at the edge, and the simulation took a significant amount of time (roughly five days on a single-processor workstation). The procedure was to dramatically overinject a uniform electron current, most of which would be turned back by space-charge effects. The overinjection would also lead to oscillations in the system, which would eventually damp out, increasing the minimum duration of the simulation. The last significant shortcoming was the lack of any programmatic interface to the simulation - offline simulations required a specified runtime at the beginning, wait for "long enough," then reload the simulation in an interactive session to extract diagnostics.

Here, we take two approaches to improving the efficiency of this same problem. First, is a field-based emission scheme, based on prior work [67]. This scheme aims to balance Gauss's law at each node with zero surface electric field ($E = 0$). The scheme is modified to account for nonzero electric field, in order to account for the effects of initial electron velocity [27], and even explore gradients in the profile of that surface field. The scheme is extended to account for errors in weighting due to cylindrical coordinates and nonzero initial velocity. The ultimate goal of this scheme is to locate the space-charge limit without the need to dramatically overinject the beam.

The second improvement is to add a layer of Python code, to allow interactive programmatic steering of the simulation [63]. This programmatic interface allows sophisticated high-level in-

teraction with the simulation, enabling a finer decision-making process. For instance, the initial approach ran for a pre-determined time, in order to ensure that oscillations in the scheme are damped out. With the Python interface, it is possible to "run until oscillations damp out," eliminating wasted cycles.

4.2   The Basic Emission Model

Following Shiffler, Cartwright *et al.*, we use Field-limited emission [67]. However, the system we simulate does not have zero initial velocity in general, so the electric-field at the cathode is not zero at the space charge limit [27]. For this, we modify the scheme such that, instead of solving Gauss's law with $E = 0$, we solve it with $E = E'$, where E' is a factor we can tune in order to optimize the transmitted current.

For each node, we solve Gauss's law

$$\oint_S \vec{E} \cdot d\vec{A} = \frac{1}{\epsilon} \int_V \rho dV, \tag{4.1}$$

where ρ is the charge density at the node, $\vec{E}$ is the electric field at the node, and $d\vec{A}$ and dV are the differential area normal to the closed surface, and volume, respectively. In discrete form, this is

$$\sum_{node_i} \vec{E} \cdot \Delta \vec{S}_n = \frac{\rho}{\epsilon} \left(\Delta V\right)_i, \tag{4.2}$$

where $\Delta \vec{S}$ and ΔV are the surface and half-cell volumes respectively. We want to satisfy this equation, so at each timestep we determine the amount of charge to be added ($Q_{G(i)}$) to the ith node to be

$$Q_{G(i)} = \sum_{node_i} \epsilon(\vec{E} - \vec{E}') \cdot \Delta \vec{S} - \rho \left(\Delta V\right)_i, \tag{4.3}$$

such that Equation (4.3) is satisfied at the ith node, and Gauss's law is balanced when $E = E'$, our tuned target surface electric field.

Equation (4.3) gives us the amount of charge that should be added at each node, but we actually distribute particles throughout the cell. There are two basic approaches to emission based on this information. First, is Primary Cell Emission (PCE), where the two surrounding node solutions for Q_G are used to determine the emission throughout a given cell, and current is interpolated linearly across the cell. An alternative is Dual Cell Emission (DCE), where the Gauss solution at a single node determines the emission in the half-cell on either side. These two approaches have been shown to be equivalent after integrating across cells, with the exception of the last half-cell [67].

We will start with PCE, where we use the Gauss-balancing Q_G at the node on either side of the cell, which we will call $Q_{G(i)}$ and $Q_{G(i+1)}$. The total charge we add to the cell is the average

$$Q_{cell(i)} = \frac{1}{2} \left(Q_{G(i)} + Q_{G(i+1)}\right). \tag{4.4}$$
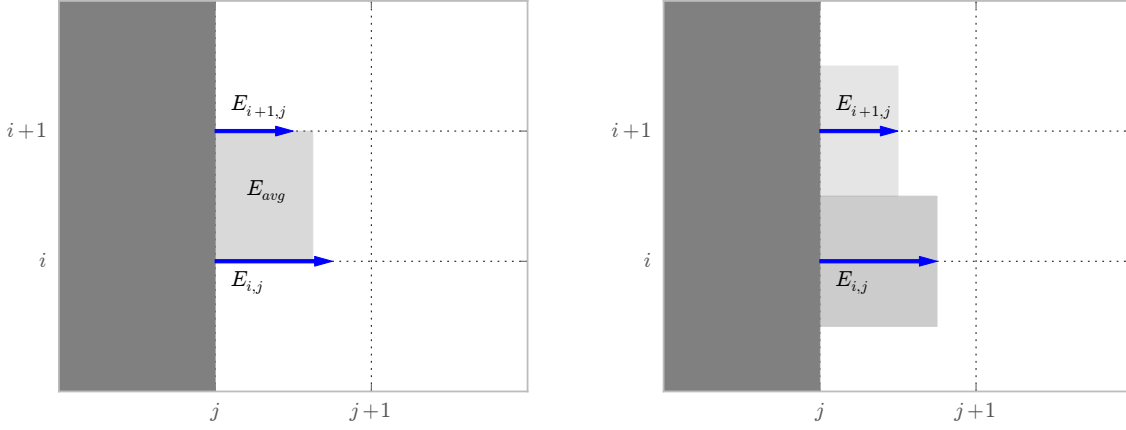
(a) PCE uses average of points surrounding cell   (b) DCE centers on the nodes

Figure 4.1: DCE and PCE emission on the Yee mesh, showing the different electric-field values used to determine the charge that should be emitted.

For a continuous emitted charge distribution $Q(x)$, we weight the particle distribution linearly across the cell, such that

$$Q(\zeta) = (1 - \zeta)Q_{G(i)} + (\zeta)Q_{G(i+1)}, \tag{4.5}$$

where

$$\zeta = \frac{x - x_i}{x_{i+1} - x_i} \tag{4.6}$$

$$\zeta(x = x_i) = 0 \tag{4.7}$$

$$\zeta(x = x_{i+1}) = 1, \tag{4.8}$$

such that ζ, normalized to 1, describes the position across the cell, and $Q(\zeta)$ describes the emitted charge distribution across the cell. This ensures that our emission profile $Q(x)$ is continuous from one cell to the next, and that $Q(x)$ matches the Gauss's law solution at each node:

$$Q(\zeta = 0) = Q(x = x_i) = Q_{G(i)} \tag{4.9}$$

$$Q(\zeta = 1) = Q(x = x_{i+1}) = Q_{G(i+1)} \tag{4.10}$$

4.3   Analysis

With the various weighting schemes, there can be a lot of values to keep track of, and since they all are various representations or approximations of Q, we will start with a notation table.

$Q(x)$ Emitted charge profile as a function of x, the position on the boundary.

$Q(\zeta)$ A segment of $Q(x)$ on a given cell, where ζ is the normalized position within the cell.

$Q_{G(i)}$ Charge that, if added, would balance Gauss's law at the ith node.

$Q_{n(i)}$ Charge weighted by the emission scheme to the ith node.

$Q_{n(i)-}$ Component of $Q_{n(i)}$ weighted from the $(i-1)$th cell.

$Q_{n(i)+}$ Component of $Q_{n(i)}$ weighted from the ith cell.

$Q_{cell(i)}$ Charge emitted in the ith cell.

$Q_{w(i)+}$ Q value used as the weight at the ith node, for emission in the cell above.

$Q_{w(i)-}$ Q value used as the weight at the ith node, for emission in the cell below.

Using linear particle weighting, the charge contribution to the node on either side of the cell is the integral of $Q(\zeta)$ times the distance:

$$Q_{n(i)+} = \int_0^1 (1-\zeta)Q(\zeta)d\zeta \tag{4.11}$$

$$Q_{n(i+1)-} = \int_0^1 \zeta Q(\zeta)d\zeta \tag{4.12}$$

Since $Q(\zeta)$ is linear, these integrals are straightforward, such that in the ith cell

$$Q_{n(i)+} = \frac{1}{3}\left[Q_{G(i)+} + \frac{1}{2}(Q_{G(i+1)})\right] \text{ and} \tag{4.13}$$

$$Q_{n(i+1)-} = \frac{1}{3}\left[Q_{G(i+1)} + \frac{1}{2}(Q_{G(i)})\right], \tag{4.14}$$

as illustrated in Figure 4.2, which we can expand to show the full charge weighted to each node:

$$Q_{n(i)-} = \frac{1}{3}\left(Q_{G(i)} + \frac{1}{2}Q_{G(i-1)}\right) \tag{4.15}$$

$$Q_{n(i)+} = \frac{1}{3}\left(Q_{G(i)} + \frac{1}{2}Q_{G(i+1)}\right) \tag{4.16}$$

$$Q_{n(i)} = Q_{n(i)-} + Q_{n(i)+} \tag{4.17}$$

$$= \frac{2}{3}Q_{G(i)} + \frac{1}{6}\left(Q_{G(i-1)} + Q_{G(i+1)}\right) \tag{4.18}$$

where $Q_{n(i)+}$ is the contribution from the cell above the ith node, and $Q_{n(i)-}$ is the contribution from the cell below the ith node. This is to say, two parts the expected charge at the node from Gauss's law, plus one part of the average of the two adjacent nodes.

We can compare the actual emitted charge weighted to the node $Q_{n(i)}$ with the expected charge $Q_{G(i)}$, to see the error in this scheme:
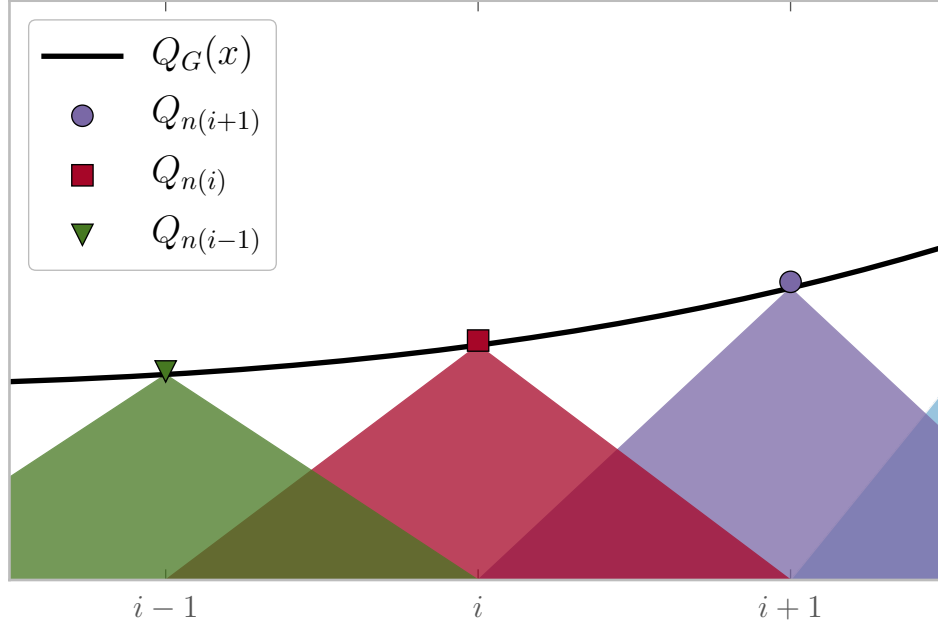
Figure 4.2: $Q_{n(i)}$ for each node with continuous-$Q(x)$ PCE weighting, which systematically over-estimates Q at each node. The colored areas indicate the area of influence for the charge weighted to each node, while the points indicate the final weighted value at each node, integrated over the two adjacent cells.

$$Q_{G(i)} - Q_{n(i)} = -\frac{1}{3}Q_{G(i)} + \frac{1}{6}\left(Q_{G(i-1)} + Q_{G(i+1)}\right) \tag{4.19}$$

$$= \frac{1}{6}\left[\left(Q_{G(i+1)} - Q_{G(i)}\right) - \left(Q_{G(i)} - Q_{G(i-1)}\right)\right], \tag{4.20}$$

and we can define a useful parameter δQ_i, the change in Q_G across the ith cell,

$$\delta Q_i = Q_{G(i)} - Q_{G(i-1)}, \tag{4.21}$$

and we see that the error in the emitted charge $Q_{n(i)}$ is one sixth of the difference between δQ across the cell before and after the node:

$$Q_{G(i)} - Q_{n(i)} = \frac{1}{6}\left(\delta Q_{i+1} - \delta Q_i\right). \tag{4.22}$$

Now, we can look at a few cases for the current profile, to examine the accuracy of this scheme.

First, in the case of uniform current the error is zero everywhere, because adjacent Q_G values are everywhere equal, so δQ is always zero. No difference, thus no error.

In the case of a linear current profile, Equation (4.20) shows that the error is in terms of the *difference* between δQ values on two adjacent nodes, which is zero for a constant slope on a uniform grid. The reason being that the current weighted to the node from the lower cell is underestimated, but the contribution from the upper cell is overestimated by the same amount.

If the current profile is any polynomial other than linear, then there will be a small error at every node, depending on how well a line approximates the profile, still assuming uniform grid.

We can look at the scaling of this error in terms of δQ_i, since every error in the emission is proportional to a point in this array. Rewriting this in terms of physical parameters,

$$Q_{G(i)} = J_i \Delta x \Delta z \Delta t \tag{4.23}$$

$$\delta Q_i = (J_i - J_{i-1}) \Delta x \Delta z \Delta t, \tag{4.24}$$

where Δx is the spatial cell size and Δt is the timestep, and J_i is the current density weighted to a given node,

$$J_i = \frac{1}{x_{i+1} - x_{i-1}} \int_{x_{i-1}}^{x_{i+1}} J(x) W(x) dx, \tag{4.25}$$

where $W(x)$ is a weighting function. A simple Taylor expansion of J_i around x_i gives

$$J_{i-1} = J_i - \frac{dJ_i}{dx} \Delta x + O(\Delta x^2), \tag{4.26}$$

so

$$J_i - J_{i-1} = \frac{dJ_i}{dx} \Delta x + O(\Delta x^2), \tag{4.27}$$

which we can plug back into Equation (4.24) to get

$$\delta Q = \frac{dJ_i}{dx} \Delta x^2 \Delta z \Delta t + O(\Delta x^3), \tag{4.28}$$

thus showing that this scheme is indeed second order accurate in Δx, and proportional to the spatial derivative of the current profile J on a uniform grid.

4.4   Particle-Weighting across a Cell

We have seen that applying PCE with linear weight based on the Q_G at each node will not actually satisfy the DCE condition. This is critically important, because a $Q_{G(i+1)}$ significantly higher than $Q_{G(i)}$ will inappropriately affect $Q_{n(i)}$, and be expressed in ρ_i in subsequent Gauss's law calculations. This ultimately causes a spatial oscillation error, overinjecting and underinjecting at every other cell. We can address this with a modification to the linear weighting scheme.

Instead of using $Q_{G(i)}$ and $Q_{G(i+1)}$ directly as the weights, we use weights $Q_{w(i)+}$ and $Q_{w(i+1)-}$, where

$$Q_{w(i)+} = \frac{1}{a-1}(aQ_{G(i)} - Q_{G(i+1)}) \text{ and} \tag{4.29}$$

$$Q_{w(i+1)-} = \frac{1}{a-1}(aQ_{G(i+1)} - Q_{G(i)}) \tag{4.30}$$

where a is a parameter to be determined. From this, we get a new form of Equation (4.5),

$$Q(\zeta) = (1-\zeta)Q_{w(i)-} + \zeta Q_{w(i)+}, \tag{4.31}$$

which is the same as Equation (4.5), just with new values for the upper and lower weights, taken from Equations (4.29)-(4.30). We divide by $(a-1)$ in order to ensure that we always satisfy the PCE condition for total particles emitted in a cell, where

$$\frac{1}{2}(Q_{w(i)+} + Q_{w(i+1)-}) = \frac{1}{2(a-1)}\left[(aQ_{G(i+1)} - Q_{G(i)}) + (aQ_{G(i)} - Q_{G(i+1)})\right] \tag{4.32}$$

$$= \frac{1}{2(a-1)}\left[(a-1)Q_{G(i)} + (a-1)Q_{G(i+1)}\right] \tag{4.33}$$

$$= \frac{1}{2}(Q_{G(i)} + Q_{G(i+1)}) \tag{4.34}$$

Now, to satisfy the DCE condition that Gauss's law is balanced at each node, we analyze the charge deposited on either side of the cell, as we did previously in Equations (4.13)-(4.14). Only this time, we use the new weights from Equations (4.29)-(4.30):

$$Q_{n(i)+} = \frac{1}{3}\left(Q_{w(i)+} + \frac{1}{2}Q_{w(i+1)-}\right) \tag{4.35}$$

$$Q_{n(i)-} = \frac{1}{3}\left(Q_{w(i+1)-} + \frac{1}{2}Q_{w(i)+}\right) \tag{4.36}$$

The DCE condition is that the actual charge deposited on each node is equal to that expected by the Gauss's law solution at that node, so for the lower node of a given cell

$$Q_{n(i)+} = \frac{1}{2}Q_{G(i)}, \tag{4.37}$$

where Q_G is halved because it is only half of the node's charge, the other half coming from the cell on the other side of the node. In order to satisfy DCE, we set Equation (4.35) equal to (4.37):

$$Q_{n(i)+} = \frac{1}{3}\left(Q_{w(i)+} + \frac{1}{2}Q_{w(i+1)-}\right) = \frac{1}{2}Q_{G(i)} \tag{4.38}$$

and plug in Equations (4.29)-(4.30), giving

$$Q_{n(i)+} = \frac{1}{3(a-1)} \left[(aQ_{G(i)} - Q_{G(i+1)}) + \frac{1}{2}((aQ_{G(i+1)} - Q_{G(i)})) \right] = \frac{1}{2}Q_{G(i)}. \tag{4.39}$$

Simplifying the algebra,

$$2(aQ_{G(i)} - Q_{G(i+1)}) + (aQ_{G(i+1)} - Q_{G(i)}) = 3(a-1)Q_{G(i)} \tag{4.40}$$

$$= (2a-1)Q_{G(i)} + (a-2)Q_{G(i+1)} = 3(a-1)Q_{G(i)}, \tag{4.41}$$

gives us two expressions for a in order for this to satisfy Gauss's law at each node independent of the relationship of $Q_{G(i)}$ and $Q_{G(i+1)}$:

$$2a - 1 = 3(a-1) \tag{4.42}$$

$$a - 2 = 0, \tag{4.43}$$

where it is apparent that the solution to both is $a = 2$. This scheme now satisfies the PCE condition for emission in each cell, and the DCE condition for current weighted to each node, assuming linear weighting. This analysis can be repeated for nearest-grid-point (NGP) weighting, where it will be found that $a = 3$ satisfies the DCE condition. The final profile for $Q(x)$ with $a = 2$ is shown in Figure 4.3.

Comparing the difference between the injected $Q_{n(i)}$ and the Gauss-balancing target $Q_{G(i)}$ for continuous $Q(x)$ (equivalent to $a = \infty$), and $Q(x)$ with $a = 1.5, 2, 3$ in Figure 4.4, we see that when a is too large $Q_{n(i)}$ is overestimated, and it is underestimated when a is too small. Weighting with $a = 2$ gives precisely the correct value [67].
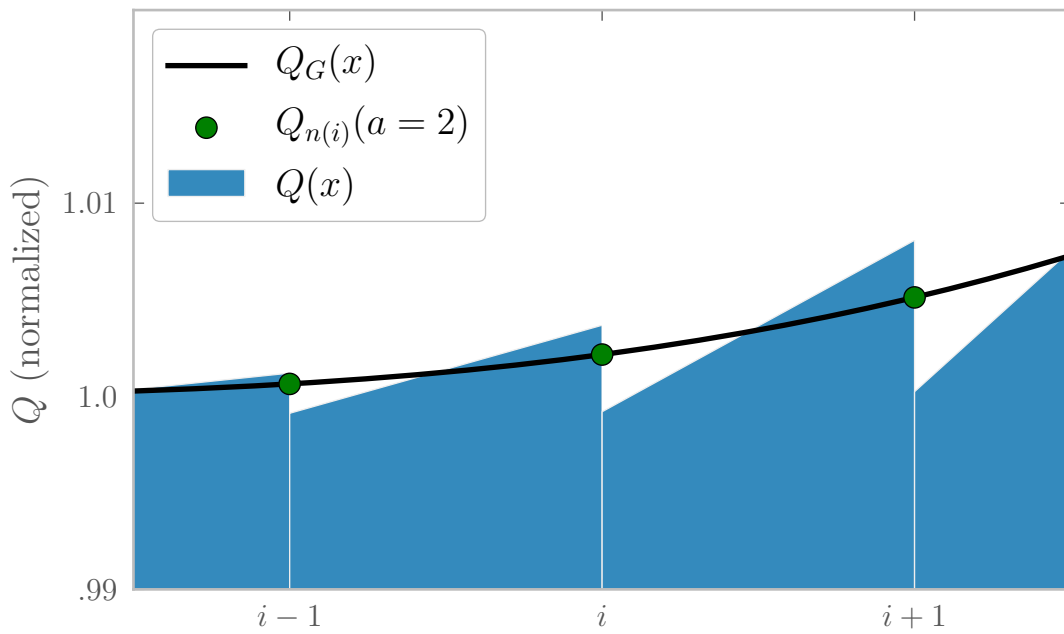
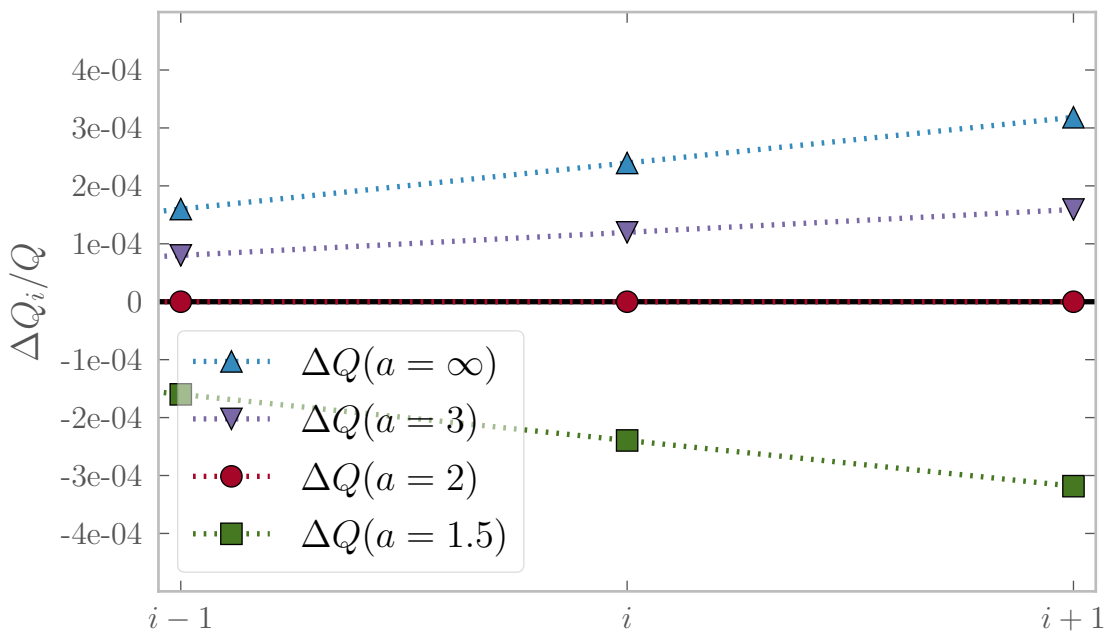Figure 4.3: Current profile for Gauss-satisfying PCE emission scheme.

Figure 4.4: Relative error in charge weighted to nodes with PCE for linear $Q(x)$.

4.5 The Last Cell

The analysis of the scheme holds true for any interior cell, but care must be taken when addressing the final cell. This is because the final $Q_{G(i+1)}$ is defined at a node whose surrounding region resides half in the edge of the beam, and half in the vacuum outside the beam. If we treated this cell as all the others, there would be significant errors.

Take the first timestep, where ρ is zero everywhere, and E is constant. Every Gauss solution will balance with the same Q_G, but the area surrounding the outermost node will only emit half the charge of interior nodes. This difference will be represented in the ρ values for future Gauss's law solutions. ρ will be half what is expected by the solutions, and Gauss's law will never balance at the outermost node because Q_n is chosen according to Equation (4.3), assuming that half of the charge will be emitted on either side of the node, which is not the case at the outermost node.

The expression in Equation (4.18) is different for the last node ($i = K + 1$),

$$Q_{n(K+1)+} = 0 \tag{4.44}$$

$$Q_{n(K+1)} = Q_{n(K+1)-} = \frac{1}{2}Q_{G(K+1)}, \tag{4.45}$$

because there is no charge deposited in the outer half-cell. The error expression in Equation (4.20) becomes the same

$$Q_{G(K+1)} - Q_{n(K+1)} = \frac{1}{2}Q_{G(K+1)}. \tag{4.46}$$

There are a few potential approaches to address this discrepancy. One would be to double the final $Q_{G(i+1)}$, such that the added charge in the last half-cell balances Gauss's law at the edge node. This approach will introduce a huge amount of current in the outermost half-cell. Before doing that, however, we must note that it is not clear that balancing Gauss's law at the edge node is actually correct. The interior scheme is based on the assumption that Gauss's law should be balanced, and that half of the charge applied to a given node will be applied on either side, which is not true ad the edge node.

We analyze two approaches to the final node:

- No special treatment ($Q_{n(K+1)} = \frac{1}{2}Q_{G(K+1)}$).

- Balance Gauss's law ($Q_{n(K+1)} = Q_{G(K+1)}$).

We can compare each of these to the continuous solution ($\Delta x \to 0$ limit). We start with a simple polynomial profile

$$J(x) = a + x^p. \tag{4.47}$$

If we normalize the beam width to $x = 1$, then we can analyze the error and convergence of each of these approaches. The exact charge deposited in the last cell should be

$$Q'_{cell(K)} = \int_{1-\Delta x}^{1} J(x) dx \Delta z \Delta t \tag{4.48}$$

$$= \Delta z \Delta t \left[a \Delta x + \frac{1}{p+1} x^{p+1} \Big|_{1-\Delta x}^{1} \right] \tag{4.49}$$

$$= \Delta z \Delta t \left[a \Delta x + \frac{1}{p+1} \left(1 - (1 - \Delta x)^{p+1} \right) \right] \tag{4.50}$$

In each of our proposed schemes for the last cell, the charge in the last cell is the simple average of the two final nodes

$$Q_{cell(K)} = \frac{\Delta x}{2} \left(Q_{n(K)} + Q_{n(K+1)} \right) \tag{4.51}$$

In the first simple case of no special treatment, we have

$$Q_{n(K+1)} = Q(1) = J(1) \Delta x \Delta z \Delta t \tag{4.52}$$

$$Q_{n(K)+} = Q(1 - \Delta x) = J(1 - \Delta x) \Delta x \Delta z \Delta t \tag{4.53}$$

$$Q_{cell(K)} = \frac{1}{2} \left(Q(1) + Q(1 - \Delta x) \right) \tag{4.54}$$

$$= \Delta z \Delta t \left[a \Delta x + \frac{\Delta x}{2} \left((1 - \Delta x)^p + 1 \right) \right] \tag{4.55}$$

Hereafter, we will set Δz and Δt to one, since they have no effect. Combining Equations (4.50) and (4.55), we get the difference between the two

$$\Delta Q_K = \frac{1}{2(1+p)} \left(-2 + (1+p)\Delta x + (1 - \Delta x)^p (2 + (p-1)\Delta x) \right) \tag{4.56}$$

Stopping here, if we plug a linear current profile ($p = 1$) into Equation (4.56), we get

$$\Delta Q_K = \frac{1}{2(1+1)} \left(-2 + (1+1)\Delta x + (1 - \Delta x)(2) \right) \tag{4.57}$$

$$= \frac{1}{4} \left(-2 + 2\Delta x + 2 - 2\Delta x \right) \tag{4.58}$$

$$= 0, \tag{4.59}$$

showing that the approximation is exactly correct for a linear profile, as should be expected. If we do a simple Taylor expansion of Equations (4.50) and (4.55) around $\Delta x = 0$, we can see that the

error

$$\Delta Q_K = \left[(1+a)\Delta x - \frac{p\Delta x^2}{2} + \frac{1}{4}p(p-1)\Delta x^3 + O(\Delta x^4) \right] \tag{4.60}$$

$$- \left[(1+a)\Delta x - \frac{p\Delta x^2}{2} + \frac{1}{6}p(p-1)\Delta x^3 + O(\Delta x^4) \right] \tag{4.61}$$

$$= \frac{1}{12}p(p-1)\Delta x^3 + O(\Delta x^4) \tag{4.62}$$

converges to third order in Δx, so the contribution will be small, since we have already shown that our scheme across the whole emission surface is second order over all. For $p > 1$, or a steep wing in the profile, ΔQ_K will be positive, slightly overestimating the current in the cell. For $p < 1$, there will be a slight underestimation of the current.

Balancing Gauss's Law

Applying the same analysis with the Gauss-balancing scheme of

$$Q_{n(K+1)-} = 2Q(1) \tag{4.63}$$

we get

$$Q_{cell(K)} = \frac{1}{2} \left(2Q(1) + Q(1 - \Delta x) \right) \tag{4.64}$$

$$= a\Delta x + \frac{\Delta x}{2} \left((1 - \Delta x)^p + 2 + a \right) \tag{4.65}$$

And performing the same Taylor expansion in Equation (4.60),

$$\Delta Q_K = \left[\frac{3}{2}(1+a)\Delta x - \frac{p\Delta x^2}{2} + \frac{1}{4}p(p-1)\Delta x^3 + O(\Delta x^4) \right] \tag{4.66}$$

$$- \left[(1+a)\Delta x - \frac{p\Delta x^2}{2} + \frac{1}{6}p(p-1)\Delta x^3 + O(\Delta x^4) \right] \tag{4.67}$$

$$= \frac{1}{2}(1+a)\Delta x + \frac{1}{12}p(p-1)\Delta x^3 + O(\Delta x^4) \tag{4.68}$$

So, while this scheme does balance Gauss's law at the final node, the current in the final cell is overestimated to first-order in Δx. Further, the error is sensitive to the absolute value of the emission a, not just its spatial variation, so it will be extremely problematic to balance Gauss's law at the final node in the case of a high intensity beam.

Thus, this scheme is not acceptable, and suggests that balancing Gauss's law is not the right thing to do at the edge node. Figure 4.5 shows the convergence in the last cell current, which is third-order for the basic scheme, and first-order for the Gauss-balancing correction. Figure 4.6 shows the error for the integral of the current, where the second-order nature of the scheme as a whole dominates the error, while the first-order Gauss-balancing scheme provides the dominating error, reducing the overall accuracy of the scheme.
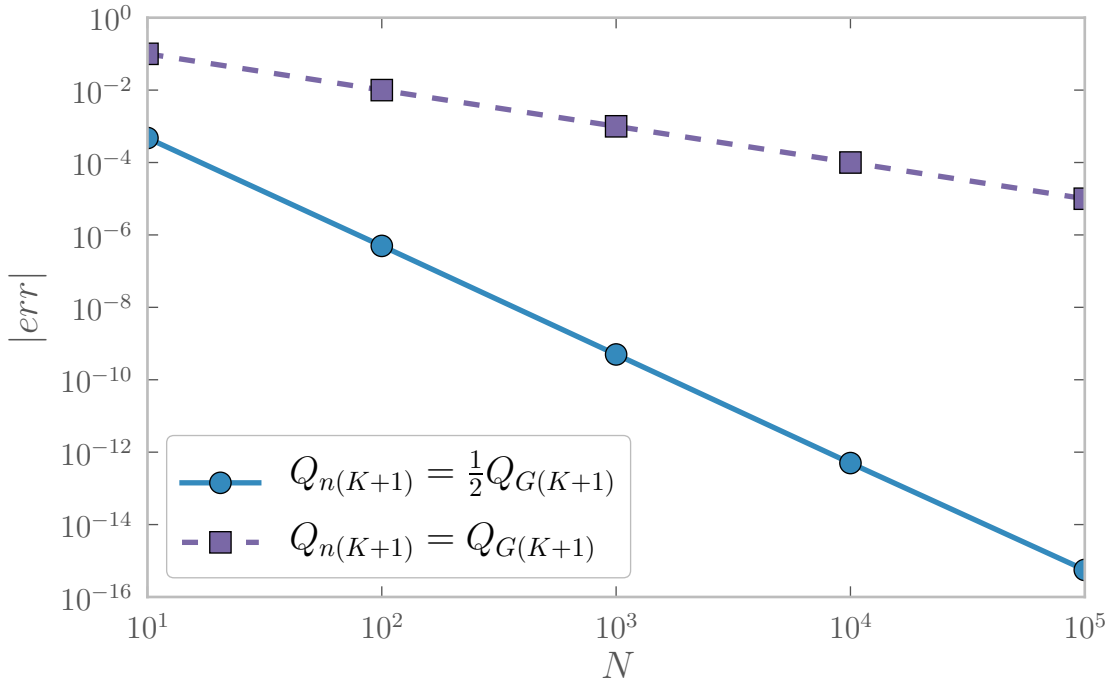
Figure 4.5: Convergence for the absolute error in the last cell for each scheme shows that balancing Gauss's law introduces an error first-order in Δx in the last cell.

Another approach

Yet another solution is to center injection on the nodes, as in DCE in general. This has no effect on any node or cell but the final one $(K + 1)$, and it increases the beam width by one half cell, as indicated in Figure 4.7, such that the last node to have an effect on the beam is now $K + 2$. What was the outermost cell (K) is now treated as a regular interior cell, and the node that defined the edge of the beam is now interior to the beam $(K + 1)$. Since the outer node is now unambiguously outside the beam,

$$Q_{G(K+2)} = 0, \tag{4.69}$$

so the total charge emitted in the last cell is $Q_{G(K+1)}/2$. The weighting described in Section 4.4 ensures that no charge is emitted in the outer half of the final cell, so that entire $Q_{G(K+1)}/2$ is weighted to node $K + 1$, resulting in the total $Q_{n(K+1)} = Q_{G(K+1)}$, fully satisfying Gauss's law at every node. In the end, this extra scheme has been deemed not to be useful, as it changes the actual width of the beam.

Ultimately, the effects of these various approaches are small, because any additional charge added in the last half-cell has a suppressing effect on the rest of the beam, resulting in no net
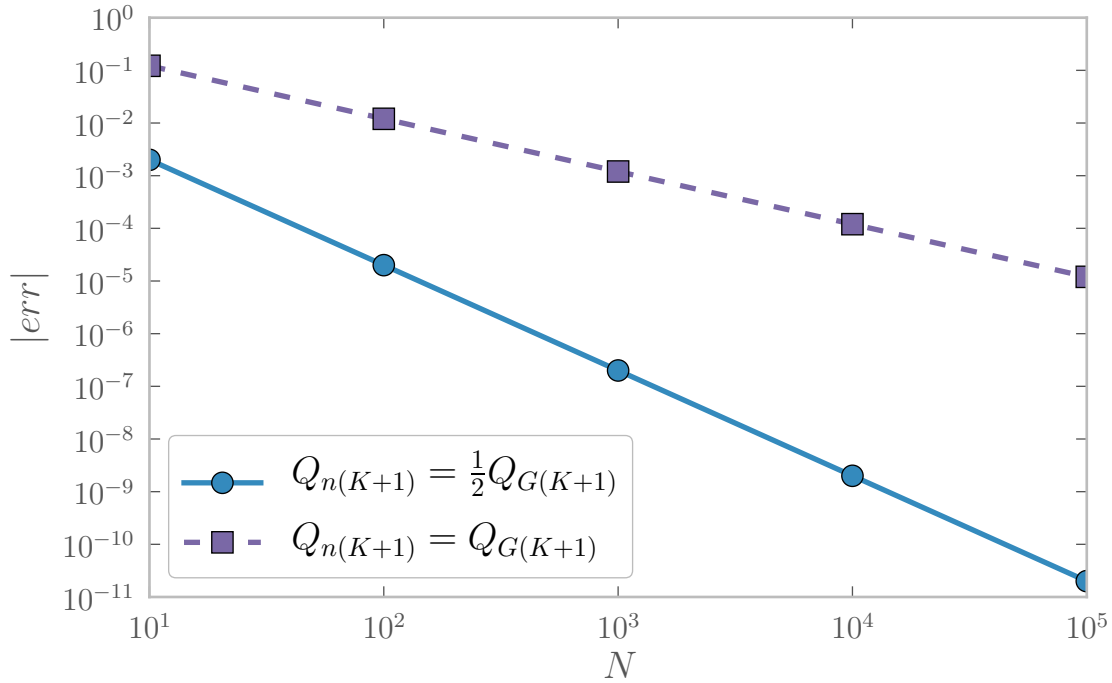
Figure 4.6: Relative error in the total current for each scheme is second order in Δx for the unadjusted scheme, and first-order for balancing Gauss's law.

enhancement of the transmitted current, but slightly redistributing J near the edge may result in other errors, such as beam interaction with a slow wave circuit, dominated by edge effects.
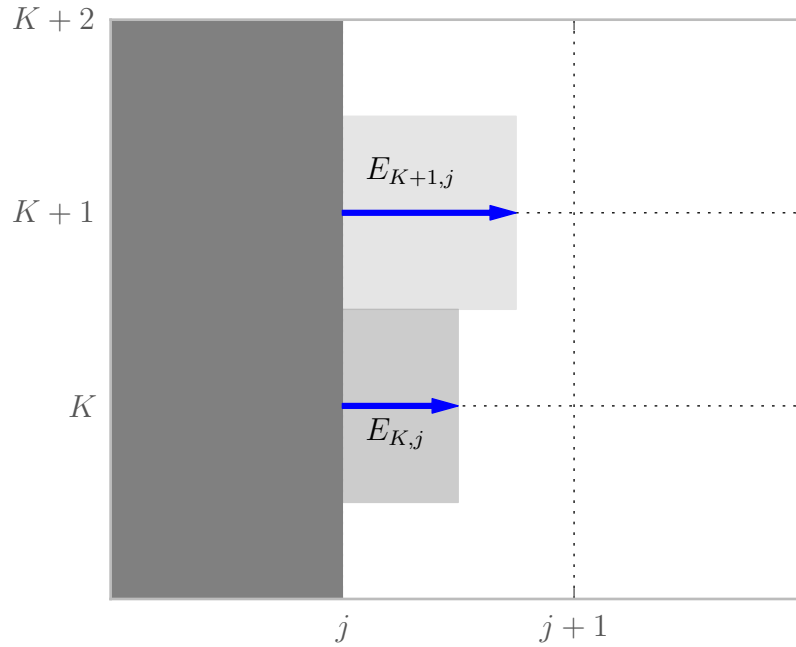
Figure 4.7: Increasing the beam width by a half cell allows balancing Gauss's law at the last $(K+1)$ node, without any additional treatment.

4.6 Cylindrical Coordinates

Our analysis this far has assumed Cartesian coordinates, but the system we actually intend to address is an axisymmetric diode, so we have to make sure the scheme works for emission as a function of radius (r). There are three steps involved in the emission process:

- Solve Gauss's law to determine $Q_{G(k)}$ at nodes

- Distribute new particles across each cell

- Weight emitted particles back to the nodes

Given a particular current profile $f(r)$, the appropriate emission has been developed previously [68]

$$
n_k = \frac{\int_r f(r) W_k(r) dr}{\int_r W_k(r) 2\pi r dr} \tag{4.70}
$$

where n_k is the particle density at node k, and $f(r)$ is the emission profile. $W_k(r)$ is the weighting
function used to weight particles to the mesh. We use linear weighting, so

$$W_{k-}(r) = \frac{r - r_{k-1}}{r_k - r_{k-1}} \qquad\qquad r_{k-1} < r < r_k \text{ and} \qquad\qquad (4.71)$$

$$W_{k+}(r) = \frac{r_{k+1} - r}{r_{k+1} - r_k} \qquad\qquad r_k < r < r_{k+1} \qquad\qquad (4.72)$$

describe the weight functions for the contribution from the lower and upper cell around node k.
So, fully expanded, Equation (4.70) becomes

$$n_k = \frac{\int_{r_{k-1}}^{r_k} f(r)\frac{r-r_{k-1}}{r_k-r_{k-1}}dr + \int_{r_k}^{r_{k+1}} f(r)\frac{r_{k+1}-r}{r_{k+1}-r_k}dr}{\int_{r_{k-1}}^{r_k} 2\pi r\frac{r-r_{k-1}}{r_k-r_{k-1}}dr + \int_{r_k}^{r_{k+1}} 2\pi r\frac{r_{k+1}-r}{r_{k+1}-r_k}dr}. \qquad (4.73)$$

The numerator is the total particles weighted to the node, and the denominator is the partial vol-
umes, integrated with the same weights. But notice that Equation (4.71)-(4.72) are identically the
ζ and $1 - \zeta$ linear weighting of the Cartesian case in Equation (4.5). So the third (weight) step is
identical to Cartesian.

Now we can analyze the distribution scheme we developed above with this information. Recall
that the distribution is defined, such that given linear weighting of a value at one node ($Q_{G(i)}$) to
that at another ($Q_{G(i+1)}$), the distribution will satisfy the condition that the total charge in the cell
is the average of the two nodes, and the charge weighted to each node is identically the input value
at those nodes. So, since we weight particles the same in cylindrical as Cartesian, we should also
distribute them the same. Thus, the only place cylindrical coordinates enter into our scheme is in
determining how many particles belong on each node. If we get that right, the rest of the scheme
should be self-consistent.

Equation (4.2) sets forth the solution to Gauss's law that determines the charge that should be
weighted to each node. Cylindrical coordinates enter in ΔV, the half-cell volumes around each
node. Now, this is simply the denominator in Equation (4.73)

$$\Delta V_k = \int_{r_{k-1}}^{r_k} 2\pi r\frac{r - r_{k-1}}{r_k - r_{k-1}}dr + \int_{r_k}^{r_{k+1}} 2\pi r\frac{r_{k+1} - r}{r_{k+1} - r_k}dr \qquad (4.74)$$

and from [68], the center and edge volumes are

$$\Delta V_0 = \int_{r_0}^{r_1} 2\pi r\frac{r_1 - r}{r_1 - r_0}dr \qquad\qquad (4.75)$$

$$\Delta V_K = \int_{r_{K-1}}^{r_K} 2\pi r\frac{r - r_{K-1}}{r_K - r_{K-1}}dr. \qquad\qquad (4.76)$$

Using these values for ΔV_k, we ensure that we have a consistent scheme in cylindrical coordinates,
satisfying Gauss's law at every node.

4.7 Initial Velocity

So far, we have assumed that particles are deposited along the boundary with no initial displacement, but this is not actually the case with nonzero initial velocity. In fact, it is not even the case for zero initial velocity.

Particles are emitted throughout the preceding timestep, so the initial position of the particle at the time of weighting is in fact, for the unmagnetized case,

$$\ddot{z}_f = \frac{q}{m} E(z(t), t) \tag{4.77}$$

$$\dot{z}_f = v' + \int_{t_n - t'}^{t_n} \frac{q}{m} E(z(t), t) dt \tag{4.78}$$

$$z_f(v', t') = \epsilon + v't' + \iint_{t_n - t'}^{t_n} \frac{q}{m} E(z(t), t) dt^2, \tag{4.79}$$

where t' is the difference between the emission time and the current simulation time, strictly less than the simulation timestep Δt, $\epsilon << \Delta z$ is the initial emission location, a very small offset from the wall, to ensure that the particle starts inside the cell, and v' is the initial velocity of the particle, such that

$$v(t_n - t') = v'. \tag{4.80}$$

z_f is the final position of the particle at the current timestep, when it will actually be weighted to the mesh. With linear weighting, the relative weight to the wall used for balancing Gauss's law is

$$1 - \frac{z_f}{\Delta z}, \tag{4.81}$$

the relative distance across the cell. This means that particles will generally end the step away from the wall, so neglecting initial velocity results in a systematic underestimation of the emission necessary to satisfy our boundary conditions.

One important case is a drifting Maxwell-Boltzmann distribution of particle velocities $f(v')$, around a uniform velocity v_0

$$f(v') = \sqrt{\frac{m}{2\pi kT}} e^{\frac{-m(v' - v_0)^2}{2kT}}, \tag{4.82}$$

and particles emitted uniformly across the timestep Δt

$$f(t') = \frac{1}{\Delta t}. \tag{4.83}$$

We need to integrate over all of the particles emitted in a given timestep, so we must integrate over the total distribution

$$f(v', t') = f(v')f(t') = \frac{1}{\Delta t} f(v') \tag{4.84}$$

in order to get the weight of particles emitted throughout the timestep

$$w = 1 - \frac{1}{\Delta t \Delta z} \int_0^{\Delta t} \int_{-\infty}^{\infty} u(z_f) z_f(v', t') f(v') dv' dt', \tag{4.85}$$

where $u(z_f)$ is a Heaviside step function, defined as

$$u(z_f) = 0 \qquad\qquad z_f < 0 \text{ and} \tag{4.86}$$
$$= 1 \qquad\qquad z_f \geq 0, \tag{4.87}$$

so that particles that would be emitted outside the system are not counted in the weight. If we take a simple test case of zero electric field everywhere, and zero electron temperature, Equation (4.79) becomes

$$z_f = v_0(t_n - t') \tag{4.88}$$

and the weight correction in Equation (4.85)

$$w = 1 - \frac{1}{\Delta t \Delta z} \frac{1}{2} v_0 (\Delta t)^2 \tag{4.89}$$
$$= 1 - \frac{v_0 \Delta t}{2 \Delta z} \tag{4.90}$$

So, when v_0 would take each particle a certain distance across the cell, the weight is one minus half of the maximum displacement for constant current, indicating an average particle position at half that distance from the wall, as one should expect.

A less trivial example to test would be the Child's law case, where the electric field is a simple function of space,

$$E(z, t) = E_0 z^{1/3}, \tag{4.91}$$

where

$$E_0 = \frac{4}{3} \frac{V}{D^{4/3}}, \tag{4.92}$$

and electrons are emitted with zero initial velocity, so

$$f(v', t') = \frac{1}{\Delta t} \delta(v'), \tag{4.93}$$

where $\delta(v')$ is the delta function. The differential equation for z in this case is

$$\frac{d^2 z}{dt^2} = A z^{1/3}, \tag{4.94}$$

where

$$A = \frac{q}{m} E_0 = \frac{4}{3} \frac{q}{m} \frac{V}{D^{4/3}}. \tag{4.95}$$

If we perform the substitution

$$v = \frac{dz}{dt} \tag{4.96}$$

$$\frac{d^2z}{dt^2} = \frac{dv}{dt} = \frac{dv}{dz}\frac{dz}{dt} = v\frac{dv}{dz}, \tag{4.97}$$

Equation (4.94) becomes the first-order differential equation

$$v\frac{dv}{dz} = Az^{1/3}, \tag{4.98}$$

which we can solve for $v(z)$, giving

$$v = \sqrt{\frac{3}{2}Az^{4/3} + C_1}, \tag{4.99}$$

where C_1 is our integration constant. But note that $v = dz/dt$, which is just our velocity, and since $v(0) = 0$ for Child's law, $C_1 = 0$, so

$$v(z) = \left(\frac{3}{2}A\right)^{\frac{1}{2}} z^{2/3}. \tag{4.100}$$

We can now plug Equation (4.96) back in for v:

$$\frac{dz}{dt} = \left(\frac{3}{2}A\right)^{\frac{1}{2}} z^{2/3}, \tag{4.101}$$

and solve for z, giving

$$z(t) = \frac{1}{27}\left[\left(\frac{3}{2}A\right)^{3/2} t^3 + 3C_2 \left(\frac{3}{2}A\right) t^2 + 3C_2^2 \left(\frac{3}{2}A\right)^{\frac{1}{2}} t + C_2^3\right], \tag{4.102}$$

where, again, initial conditions set $C_2 = 0$, so we get

$$z(t) = \frac{1}{27}\left(\frac{3}{2}A\right)^{3/2} t^3, \tag{4.103}$$

our final expression for position as a function of time since emission. Now we can plug Equations (4.93) and (4.103) into our weighting function in Equation (4.85), to get

$$w = 1 - \frac{1}{\Delta t \Delta z} \int_0^{\Delta t} \int_{-\infty}^{\infty} \delta(z_f) z_f(v', t') f(v') dv' dt' \tag{4.104}$$

$$= 1 - \frac{1}{\Delta t \Delta z} \int_0^{\Delta t} \frac{1}{27}\left(\frac{3}{2}A\right)^{3/2} t'^3 dt' \tag{4.105}$$

$$= 1 - \frac{1}{108}\left(\frac{3}{2}A\right)^{3/2} \frac{\Delta t^3}{\Delta z}, \tag{4.106}$$
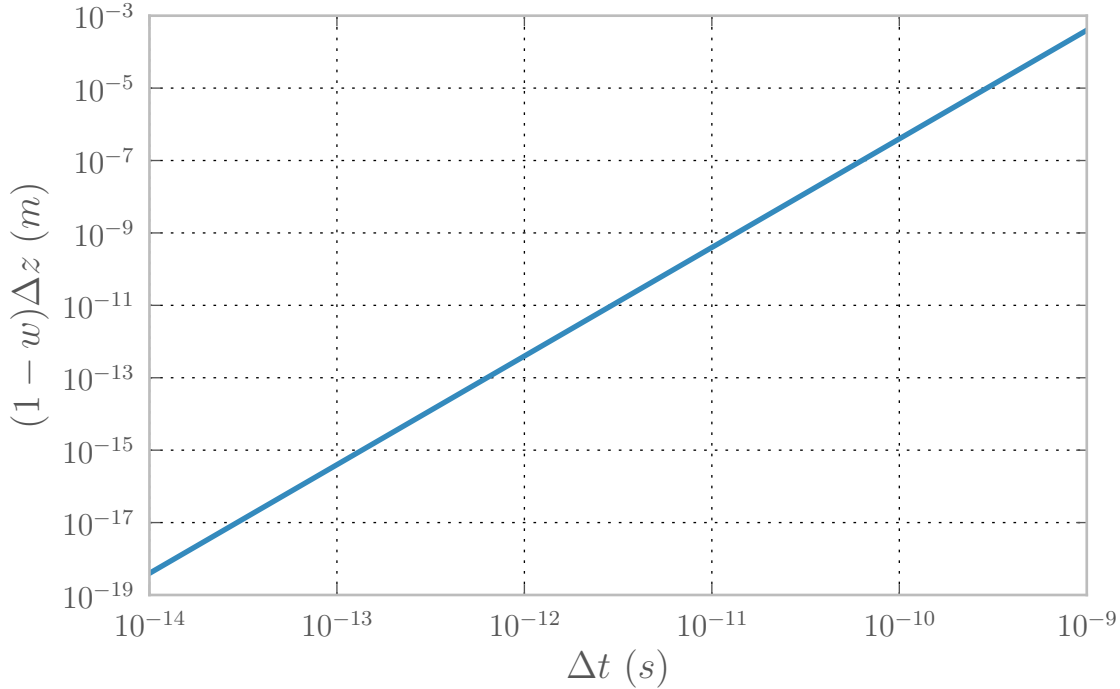
Figure 4.8: The weight correction $(1 - w)$ for Child's law emission, with $V = 1kV$ and $D = 1cm$. The correction is quite small as long as $\Delta t < 1ps$, depending on the cell size. If the cell size is large relative to the timestep, the correction becomes quite important.

and now we can plug in Equation (4.95) for A, giving our final weight

$$w = 1 - \frac{1}{108}\left(2\frac{q}{m}\frac{V}{D^{4/3}}\right)^{3/2}\frac{\Delta t^3}{\Delta z}. \tag{4.107}$$

Plugging in values we used in simulations in Chapter 2, emitting electrons across a gap separation of $D = 1cm$, and gap potential $V = 1kV$, we can plot the weight correction $(1 - w)$ for a variety of values of Δt and Δz in this system. Figure 4.8 shows that the correction is quite small, except for large timesteps and/or small cell size, for instance a timestep $\Delta t = 100ps$ and cell size of $\Delta z = 1m$, the error is more than half, so emitted current will be underinjected significantly. However, since the correction scales with Δt^3, a small reduction in timestep dramatically reduces the size of the correction, so reducing the timestep by one order of magnitude to $\Delta t = 10ps$ reduces the correction well below one tenth of one percent. An initial velocity can increase the error significantly, particularly in the case of high gradient field emission.

Applying the correction

Applying this correction in practice is straightforward. The scheme thus far will give us the number of particles that should be weighted to the wall. We use this as our starting condition N. Each time we emit and push a particle, rather than taking a unit value out of the target, we take the *weighted* value of that particle's destination $(1 - x)$. So if particles arrive halfway across a cell, then on average $2N$ particles will be emitted, rather than N. The only remaining factor to consider is to adjust the stop condition for the iteration. Previously, it was while the remaining number of particles to emit is at least 0.5, so that the error in discrete particles is centered on N. Instead, we take the expected weight of an average particle as the limit, rather than unity, so the stop condition is when the remaining number of particles to emit drops below $0.5\langle w \rangle$. This value is calculated following previous work, taking into account temporal variations in the electric field, and time-centering the velocity for a leap-frog method, ensuring second order accuracy [69]. Ultimately, it amounts to a full emission of a test particle at the average velocity v_0, and measuring its resulting position as the weight factor.

For PIC, we use the leap-frog advance to push particles, where velocities are defined at half-timesteps, and position is defined at whole timesteps, so the equations of motion (for the unmagnetized case) become

$$\mathbf{v}_{n+1/2} = \mathbf{v}_{n-1/2} + \mathbf{e}(z_n, t_n)\Delta t \tag{4.108}$$

$$\mathbf{x}_{n+1} = \mathbf{x}_n + \mathbf{v}_{n+1/2}\Delta t, \tag{4.109}$$

where $\mathbf{e} = q\mathbf{E}/m$. But this means we need to make some corrections to the emission to keep it second-order accurate, since our initial velocity and position are defined at the same time, rather than half-timestep offsets [69]. In general, the time offset of positions and velocities will be called s, where the standard case illustrated above is $s = 1/2$. We also define g, the fractional timestep before t_n at which the particle is emitted, such that

$$t' = g\Delta t, \tag{4.110}$$

so

$$\mathbf{x}_{n-g} = \epsilon \tag{4.111}$$

$$\mathbf{v}_{n-g} = v \tag{4.112}$$

our starting position and velocity at the boundary. To bring our velocity and position in-line, so they can be used in the rest of the scheme, we define

$$\mathbf{v}_{n-s} = \mathbf{v}_{n-g} + (g - s)\mathbf{e}_v\Delta t \tag{4.113}$$

and

$$\mathbf{x}_n = \mathbf{x}_{n-g} + g\mathbf{v}'_{n-g/2}\Delta t, \tag{4.114}$$

where

$$\mathbf{e}_v = (1-d)\mathbf{e}(\mathbf{x}_{n-g}, t_{n-1}) + d\mathbf{e}(\mathbf{x}_{n-g}, t_{n-2}) + (d+1-s)(\mathbf{v}_{n-g} \cdot \nabla)\mathbf{e}(\mathbf{x}_{n-g}, t_{n-1})\Delta t \quad (4.115)$$

$$d = \frac{g+s}{2} - 1 \quad (4.116)$$

$$\mathbf{v}'_{n-g/2} = \mathbf{v}_{n-g} + \frac{1}{2}g\left[\mathbf{e}(\mathbf{x}_{n-g}, t_{n-1})\right]\Delta t, \quad (4.117)$$

So we now have our initial position and velocity, defined at the right points in time for the rest of the leap-frog scheme. We use this final position x_n for the weight when measuring each particle's contribution to the target emission.

4.8   Locating E'

Having established a basic model for current injection that will maintain a given E', we can now set out to determine the value for E' that will maximize the transmitted current. We do this with a simple iteration scheme, illustrated in Figure 4.9. We start with $E' = 0$ and iterate. First, we run the simulation with $E = E'$ for a number of electron transits (2-4), then continue, measuring the output current at the anode. When anode current stabilizes, indicating a steady state, the output current is recorded, and E' is increased by a fixed amount. Once increasing E' ceases to increase the output current, this sets an upper bound on the optimal E', and we proceed to sweep E' down in the same manner, with a smaller step. This iteration proceeds until E' is known within a specified tolerance, *e.g.* one percent.

Implementation

To implement this scheme, the two-dimensional Particle-in-cell simulation code OOPIC has been wrapped in a Python interface [6]. As in Chapter 3, the underlying C++ implementation of physics and diagnostics is exposed in a non-copying manner via Cython and numpy [7] [64], enabling access to the many scientific visualization and analysis tools of the scientific Python community [66] [65].

The high-level logic of decision-making in Figure 4.9 is implemented in the Python language, allowing rapid prototyping and iterative development, without significantly impacting the inner simulation performance.
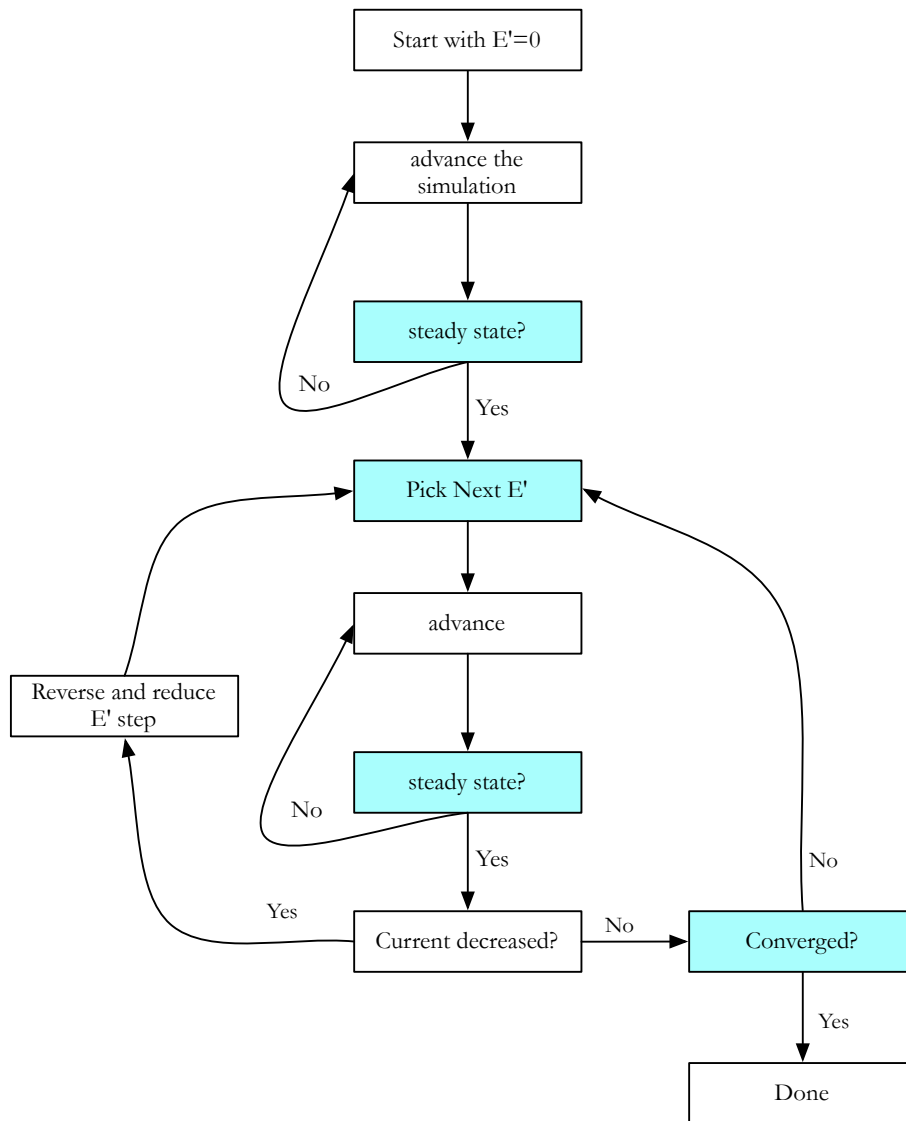
Figure 4.9: The iteration scheme for locating E'.
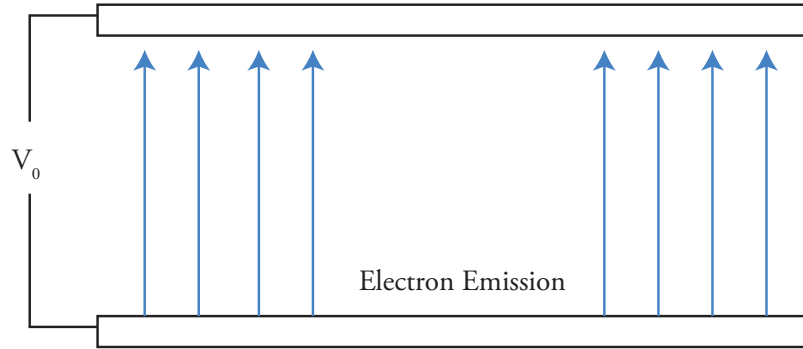
4.9 Results and Discussion

Figure 4.10: Infinite parallel plate diode.

The first result, to verify our scheme, is the one-dimensional case illustrated in Figure 4.10. We simulate an infinite parallel plate diode, with gap separation $D = 1cm$, gap potential $V = 1kV$, and initial drift energy of one to four percent the gap potential ($KE = 10 - 40eV$). The Jaffe correction

$$\frac{J_{1DSCL}}{J_{CL}} = \left(\left(1 + \frac{KE}{V}\right)^{\frac{1}{2}} + \frac{KE^{\frac{1}{2}}}{V} \right)^3 \tag{4.118}$$

to the space-charge limit in this regime ranges from $35 - 80\%$. This is achieved in a 2D simulation with periodic boundary conditions in the transverse dimension. Using the emission scheme with cathode surface field $E = 0$, we find an underestimation of the Jaffe limit by two to nine percent. It is important to note that $E' = 0$ does not result in emitting the 1D Child-Langmuir limit, rather it is significantly enhanced, though the enhancement is not fully what the Jaffe theory predicts. Applying our scheme to locate a nonzero surface field E' closes the gap between the $E = 0$ case and the Jaffe limit, as seen in Figure 4.11.
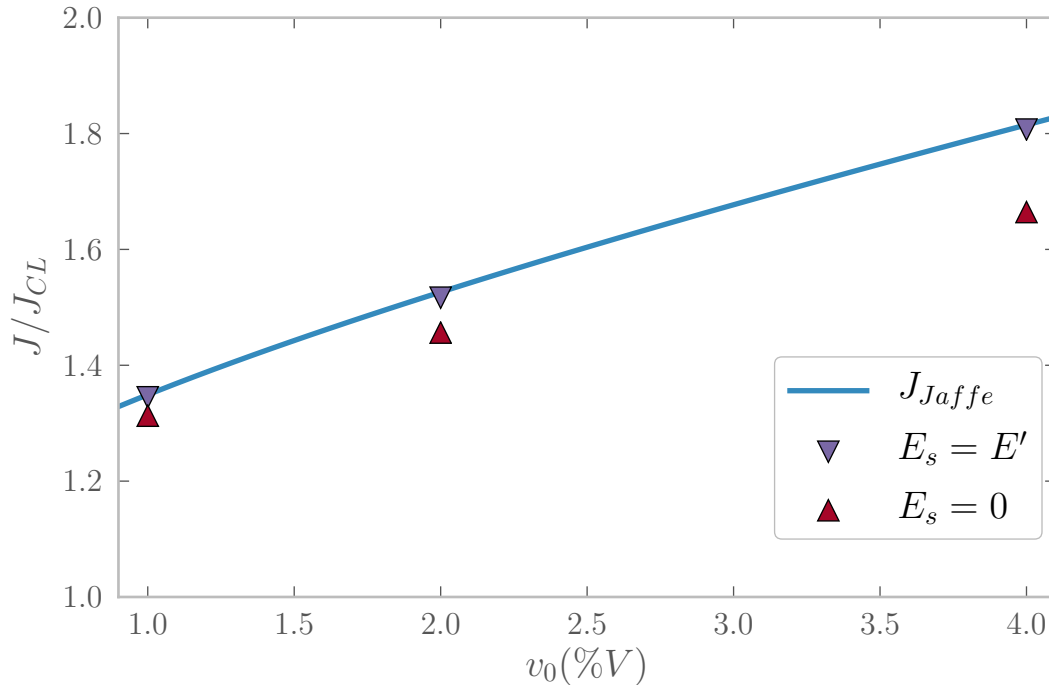
Figure 4.11: Transmitted current with $E = 0$ and $E = E'$ for infinite diode.

Having established that the scheme does produce the result expected by theory in the one-dimensional case, we can proceed to the actual motivating case - a new approach to the two-dimensional axisymmetric scaling law developed in Chapter 2. As in Chapter 2, we simulate the system described in Figure 2.1, with aspect ratio r/L ranging from 1-8. Applying the scheme described in Section 4.8, we do indeed find good agreement with prior results for an axisymmetric scaling law [44] via a very different scheme.

As in the one-dimensional case, $E = 0$ injection will systematically underestimate the space-charge limit. By adding a positive electric field, we are able to close the gap between field-limited emission and the space-charge limit, shown in Figure 4.12, where agreement between the iterative scheme and the overinjection scheme is good.

We also see in Figure 4.13 the familiar current wings and center-dip, characteristic of the current profile from our previous 2DCL approach, further validating the approach.
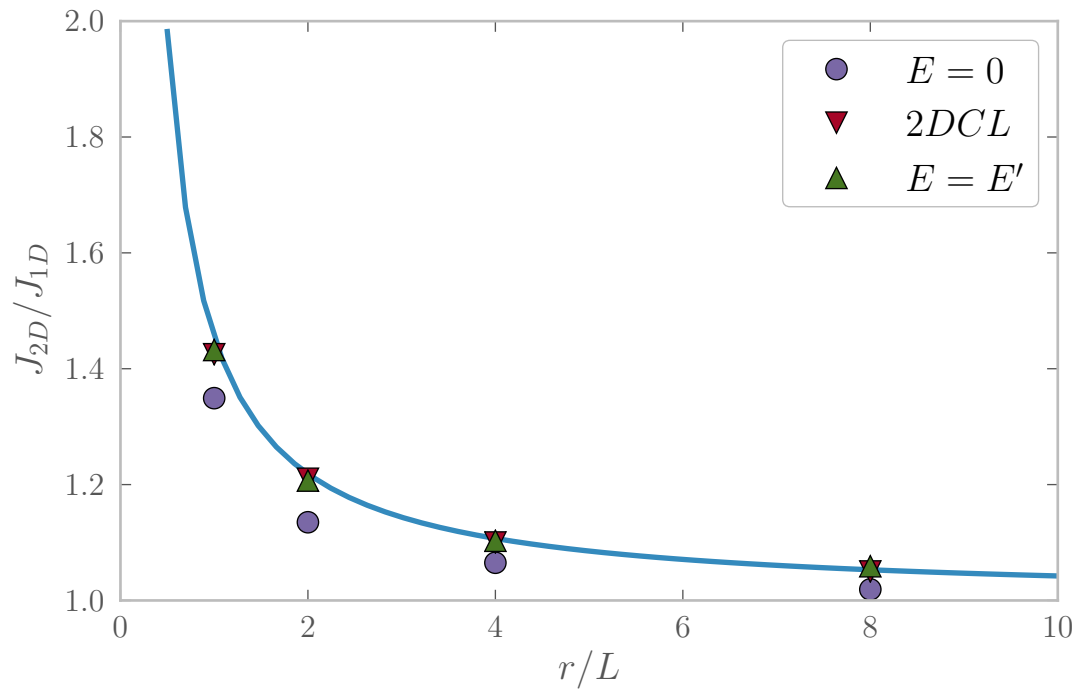
Figure 4.12: Axisymmetric scaling laws with $E = 0$ and $E = E'$. The line shows the polynomial fit to the $2DCL$ data collected in Chapter 2
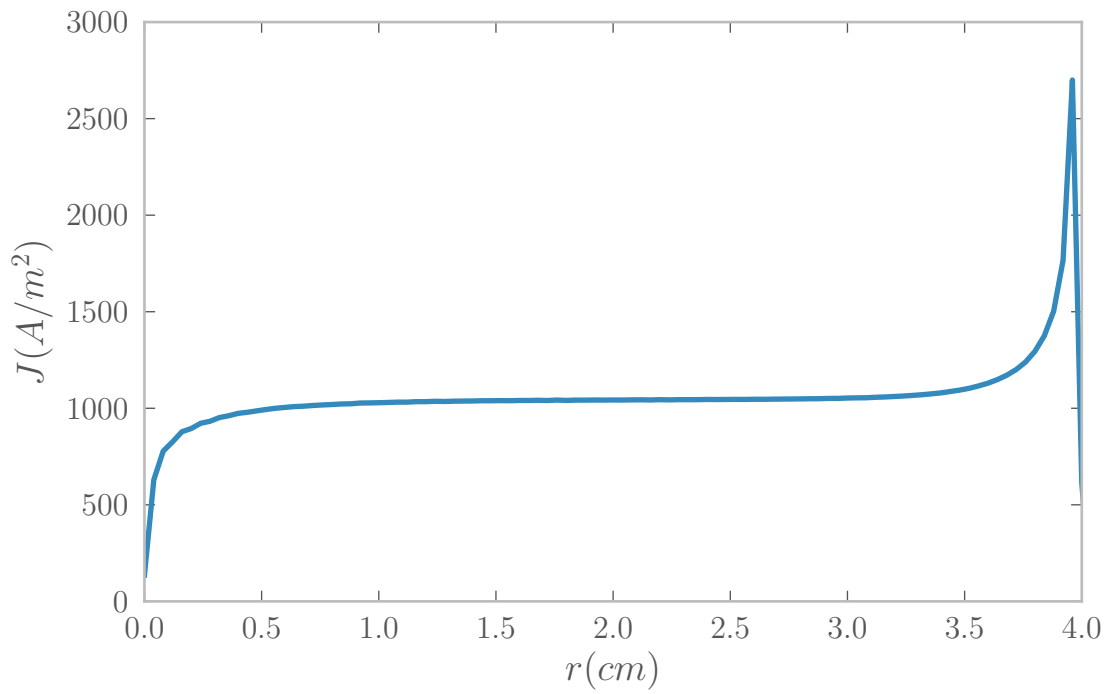
.

Figure 4.13: Anode current profile for $r/L = 4$.

4.10   Variations

Field Profile

In the case of zero initial velocity, it is obvious that the SCL implies an electric field of zero everywhere on the cathode. However, when allowing for finite initial velocity, this is no longer immediately apparent, but our scheme is not sensitive to spatial variations in E'. We can make a test case, by applying local enhancement effects of E-field profile at the center and edge of the beam. The effects of local enhancement at the center of the beam can be seen in Figure 4.14. Comparing the profile shows no discernible difference resulting from the stronger E-field at the center. The only difference appears to be an accumulation of electrons at the potential minimum, near the axis, which ultimately has no effect on the total transmitted current or its profile.

Similarly, enhancing the surface electric field at the edge of the beam, with an Electric-field profile that matches that of the transmitted current, does not have an apparent effect on the total transmitted current. It does, however, have a very small effect on the profile, slightly enhancing the peaks of the wings, but at the expense of the width of the wings, ultimately having no effect on the total current, as illustrated in Figure 4.15a
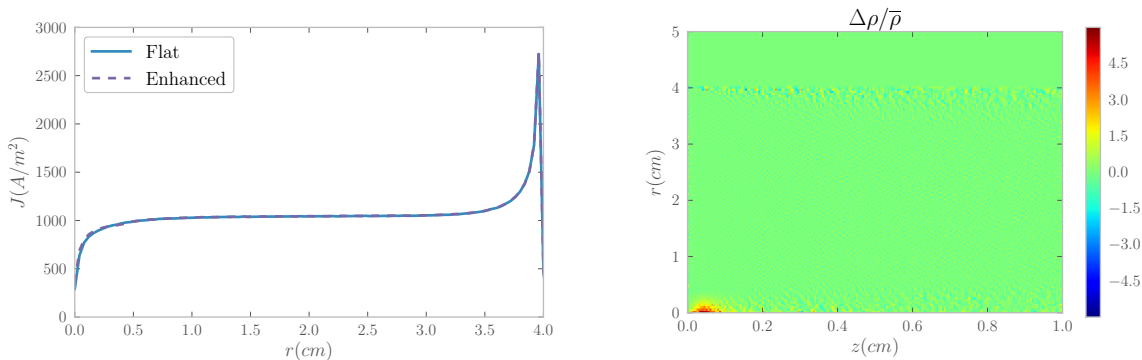
(a) Current profile for flat E' and $E'(r)$ with local enhancement on-axis.

(b) Difference in charge density (ρ).

Figure 4.14: Effects of locally enhanced E-field on-axis.

(a) Current profile for flat E' and $E'(r)$ with local enhancement at the beam edge.

(b) Difference in charge density (ρ).
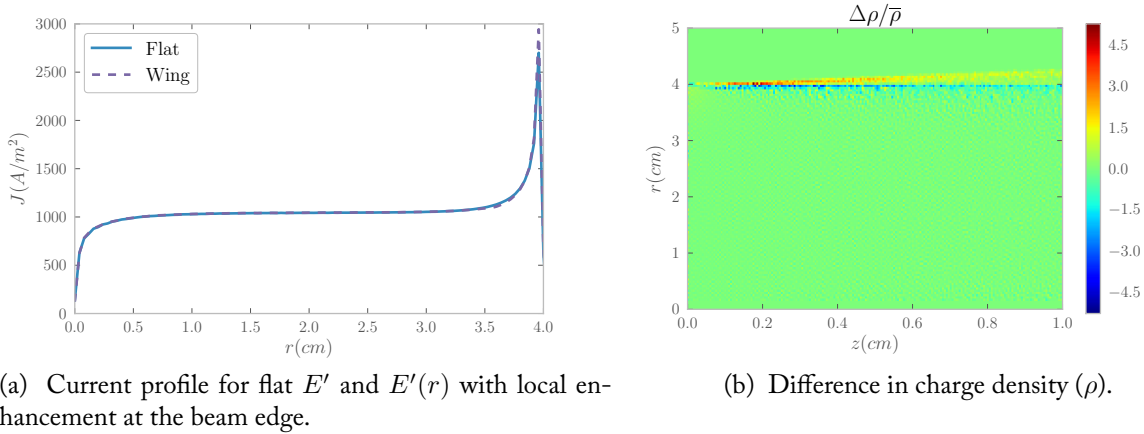
Figure 4.15: Effects of locally enhanced E-field at beam edge.

Removing the Magnetic Field Confinement

In all of these cases, we confine radial motion of the electrons by applying an infinite magnetic field. We can explore this effect by eliminating this magnetic field, and observing the effects of the confinement. Figure 4.16 shows the spread of the beam, where the high current density in the wings is allowed to spread when the B-field is relaxed. The difference in potential shows the space-charge effects pushing the beam out from the center.

Ultimately, relaxing the B-field results in the wings spreading out, and the current profile flattening (Figure 4.17). Recall from Figure 4.3, that the actual current profile is a sawtooth pattern, in order to satisfy the DCE and PCE conditions simultaneously. The severity of the sawtooth is proportional to the relative difference between each pair of nodes. If the weights assigned to two

(a) $\Delta\Phi$

(b) $\Delta\rho$

Figure 4.16: Difference in potential (Φ) and charge density (ρ) for $B = 0$ and $B = 100T$.
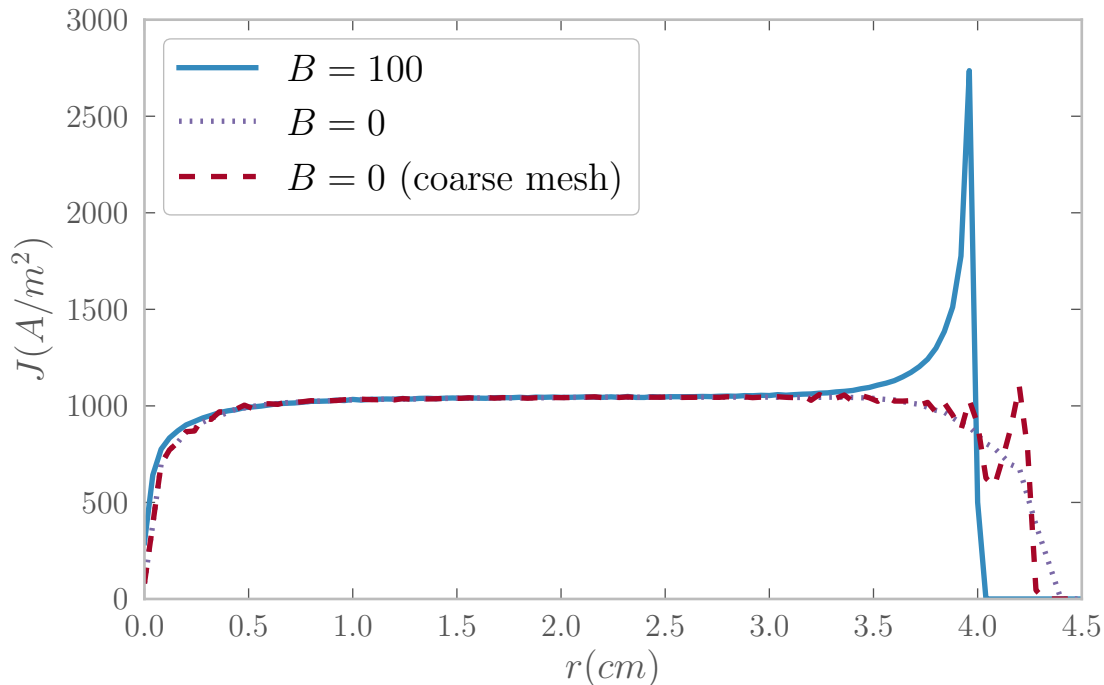
Figure 4.17: Current profile with $B = 0$. The dashed line indicates a run with insufficient grid resolution to prevent a small gap in the beam, which grows as the beam crosses the diode.

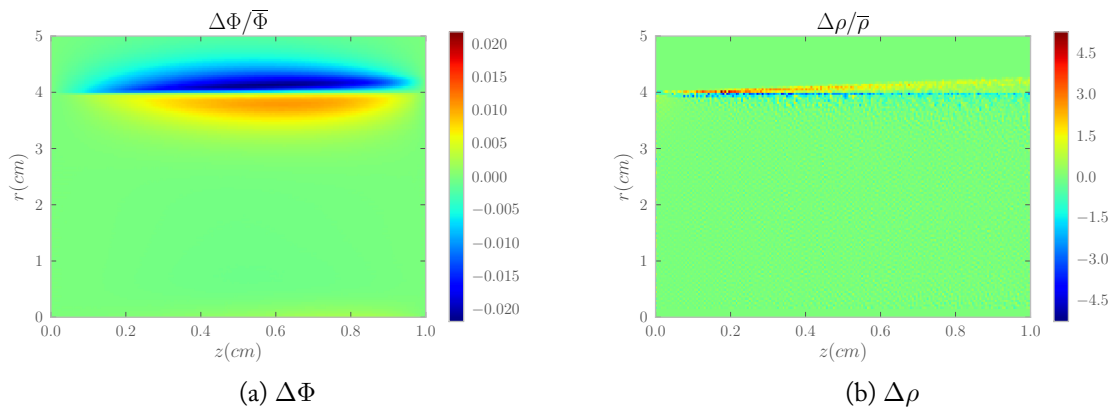adjacent nodes differ by a factor greater than two, then there will actually be a gap in the beam near the lower value. When the magnetic field is relaxed, the sawtooth pattern is allowed to spread, and is observed at the anode, and the gap in the beam near the outer edge is observed in the dashed line in Figure 4.17 To alleviate this, the mesh must be refined to minimize the sawtooth slope, at which point a simple smoothing of the profile is observed. The total transmitted current does not change significantly, as the spread beam does not have a significant effect on the surface field at the cathode, which determines the current injection. An increase in total transmitted current of one percent is observed.

4.11 Conclusions

We have extended previous work on field-based emission, taking care to preserve consistency in cylindrical coordinates and at the edge cells, and specifically analyzing alternate approaches that are ultimately deemed inappropriate. Starting with prior work that ensures Gauss's law is balanced at nodes and cells, the scheme is extended to preserve this condition in cylindrical coordinates, taking particular care at the edge and center of the beam, where prior errors have been known to occur. We further relax assumptions by accounting for nonzero velocity in the emission, which

previously would produce a systematic underestimation of the current needed to balance Gauss's law. In analyzing this velocity correction, we find it to be quite small for the Child's law regimes that we have explored, but can be large for finite initial velocities or high gradient field emission. Further analysis is provided, showing that the scheme is second-order accurate at every node, including on-axis and at the edge of the beam in cylindrical coordinates. It is our finding that forcing Gauss's law to balance at the edge node will not result in an accurate result, despite the fact that it will balance in the continuous limit. The scheme is validated in the one-dimensional case via periodic boundary conditions, and prior results recovered for the two-dimensional axisymmetric scaling law.

The iterative approach to this same result has proven dramatically more efficient than prior work described in Chapter 2. Rather than attempting to inject a uniform beam with a current dramatically exceeding the limit, our new scheme does not overinject at all. Instead, our scheme stays very near the current limit (within ten percent) throughout iteration, which means pushing eighty percent fewer particles, and a result is found in fewer timesteps. This has indeed proven significantly more efficient than the previous brute-force approach. Fewer particles are emitted, fewer timesteps are taken, and a more detailed understanding of the system is achieved.

This more efficient scheme has also allowed further exploration into the finer detail of the system, not previously achieved. The effects of the magnetic confinement, assumed to be the case in all prior simulations, is suggested to have an effect only on the current profile transmitted at the anode, but not the total transmitted current. It was suspected that local enhancements of the field at the wings, such that the surface field might reflect the profile of the current, but this has turned out not to be the case. Local field enhancements only seem to shift the profile, again not changing the total transmitted current.

Chapter 5

Conclusions

5.1 Extensions of Child's Law

We have seen a few physical results, extending our understanding of space-charge effects on current through a circular parallel plate diode with finite radius. In Chapter 2, we developed a new scaling law for axisymmetric geometry, which has been shown to agree well with experiment [4], and extended prior work in planar geometry [2]. We find a scaling law for the maximum space charge limited steady-state current density, which scales as r/L relative to the predictions of 1D analytic solutions. We also develop a theoretical model to support these results in both geometries, and a take on a geometric analysis on the relative contribution of the current density peaks at the outer edge of the beam. These 'wings' are found to have a fixed width, independent of the width of the beam. Our approach converges to the one-dimensional limit slower than other, similar work [45], and it is suggested that the contribution from the current-density wings may be responsible for this slower convergence. One anomaly that continues to elude analysis is a region of low current density in the center of the beam. No analytic model has predicted this in the current profile, but the contribution to the overall emitted current is very small.

Chapter 4 took us deeper into the surface field of the same system, by following a different approach to emission. Instead of overinjecting everywhere, as in Chapter 2, we balance Gauss's law at the surface, to eliminate any overinjection. The new results agreed well with the earlier approach, but it allowed further exploration into the profile and field characteristics, due to the use of a new, more programmable Python interface. We showed that local enhancements to the surface field at both the edge and the center of the beam do not have significant effects on the total emitted current, and that the electric-field profile for space-charge-limited current is flat, unlike the current profile, which has wings at the edge and a dip in the center. Chapter 3 explored the enhancement effects of upstream ions mitigating space-charge limits across relativistic and non-relativistic energy regimes, with an analytic solution, and confirmation by simulation.

5.2 Field Emission Scheme

Chapter 4 showed the development of a comprehensive scheme for a consistent field-emission scheme based on balancing Gauss's law in two-dimensional systems. By taking prior work, and extending it to carefully account for conditions at edge and center cells, as well as nonzero initial injection velocity and particle weighting, we should have a scheme that is applicable in a wide variety of systems. The scheme is shown to recover Jaffe's space-charge-limit for an infinite parallel plate diode, and the scaling law developed in Chapter 2. Error analysis also shows the scheme to be second-order accurate at every node in both Cartesian and Cylindrical coordinates.

5.3 Simulation Tools and Techniques

We have wrapped the PTSG-developed C++ simulation codes OOPIC and OOPD1 in a Python interface, which has enabled dramatically improved interaction and analysis. In Chapter 3, we showed a feedback-based scheme for optimizing transmitted electron current based on upstream ion injection. This was done with the one-dimensional code OOPD1. We also found a useful application of mass-scaling to further improve simulation efficiency, when simulation time scales with transit time, which, in turn, scales with the ion mass.

  We took this to two-dimensions with OOPIC in Chapter 4, where we automated the axisymmetric parallel-plate diode, optimizing the transmitted current by tuning the surface field at the cathode.

  The choice of Python for the interface here is not significant on its own, as almost any programming language has the capacity to use the physics codes now that they have been exposed as dynamic libraries. Python was chosen for the ecosystem of tools around data analysis and visualization, which is particularly strong, and this decision has proven quite fruitful.

  Of particular value were the packages Cython, NumPy, matplotlib, and IPython. Cython makes the transition layer from C to Python particularly seamless, and allowed the avoidance of many of the performance penalties of native Python code. NumPy is known as the *Lingua Franca* of scientific Python, allowing easy and efficient access to a huge number of analysis tools. The IPython Notebook, in particular, allowed for a document-based approach, which facilitated collaboration and communication of results, and recording the history of each simulation run. All of the figures in this dissertation (excluding schematic diagrams) were produced with matplotlib in the IPython Notebook. Using NumPy, matplotlib, and the IPython Notebook makes for an extremely efficient workflow from running simulations to final figures for publication. The main takeaway here is that tools are of great scientific importance, as they strongly influence the actual research that is feasible.

5.4 Future Work

While this work has answered some questions, the value of a successful scientific endeavor is often in the new questions it raises more than the answers it provides. The two-dimensional axisymmetric scaling law has now been approached a few times [44] [45]. Li's work differed from ours, in that the

emitted electrons had zero velocity, whereas our approach used a finite injection velocity, requiring the potential minimum to be resolved by a fine mesh. This means that while Li's work converged to Child's law itself, ours converged to Jaffe's correction for a finite initial velocity. The result is a modest disagreement in the scaling law with respect to the aspect-ratio r/L. What remains to be done is to investigate any relationship the initial velocity may have on the scaling law. It is possible that the scaling law, even relative to Jaffe's correction, is a function of both r/L and mv_0^2/V.

Almost all of these simulations have been done with infinite magnetic field, confining the particles to longitudinal motion. While one example of relaxing the magnetic field has been shown, there is still much to learn about the possible effects of the magnetic field. Such examples may include finite magnetic fields, or even transverse fields, relevant to crossed-field devices such as magnetrons.

We have explored a couple of boundary conditions for these systems. In all cases, we held the anode and cathode to be conductors at a fixed potential, but there are other options to explore, such as floating conductors, dielectrics, or open boundaries.

While we have shown two simple and useful applications of the Python-wrapped codes, providing schemes for optimization of input parameters, there are many other physical systems and optimization schemes to which it may be applied. This is perhaps where the greatest amount of future work is to be done: Using the new, more general, tools to more easily experiment with optimizing physical parameters of other systems.

Bibliography

[1] C. D. Child, Discharge from hot CaO, *Physical Review (Series I)* **32**, 492–511 (1911).

[2] J. W. Luginsland, Y. Y. Lau, and R. M. Gilgenbach, Two-dimensional Child-Langmuir law, *Physical Review Letters* **77**, 4668–4670 (1996).

[3] W. S. Koh, L. K. Ang, and T. J. T. Kwan, Three-dimensional Child–Langmuir law for uniform hot electron emission, *Physics of Plasmas* **12**, 053107 (2005).

[4] A. Valfells, D. W. Feldman, M. Virgo, *et al.*, Effects of pulse-length and emitter area on virtual cathode formation in electron guns, *Physics of Plasmas* **9**, 2377–2382 (2002).

[5] A. Friedman, D. P. Grote, D. A. Callahan, *et al.*, Overview of WARP, a particle code for heavy ion fusion, *AIP Conference Proceedings* **297**, 347–356 (1993).

[6] J. P. Verboncoeur, A. B. Langdon, and N. T. Gladd, An object-oriented electromagnetic PIC code, *Computer Physics Communications* **87**, 199–211 (1995).

[7] S. Behnel, R. Bradshaw, *et al.*, Cython: the best of both worlds, *Computing in Science & Engineering* **13**, 31–39 (2011).

[8] J. R. Pierce, *Theory and Design of Electron Beams* (New York: Van Nostrand, 1954) Chap. 10.

[9] K. H. Kingdon, A method for the neutralization of electron space charge by positive ionization at very low gas pressures, *Physical Review* **21**, 408–418 (1923).

[10] K. T. Compton and P. M. Morse, Theory of normal cathode fall in glow discharges, *Physical Review* **30**, 305–317 (1927).

[11] R. Fowler and L. Nordheim, Electron emission in intense electric fields, *Proceedings of the Royal Society of London A* **119**, 173–181 (1928).

[12] K. F. Herzfeld, The influence of surface conditions and space charges on the conductivity of poor conductors, *Physical Review* **34**, 791–807 (1929).

[13] H. F. Ivey, Cathode field in diodes under partial space-charge conditions, *Physical Review* **76**, 554–558 (1949).

[14] J. P. Barbour, W. W. Dolan, J. K. Trolan, *et al.*, Space-charge effects in field emission, *Physical Review* **92**, 45–51 (1953).

[15] W. Shockley and R. C. Prim, Space-charge limited emission in semiconductors, *Physical Review* **90**, 753–758 (1953).

[16] A. Rose, Space-charge-limited currents in solids, *Physical Review* **97**, 1538–1544 (1955).

[17] J. Sworakowski and G. F. L. Ferreira, Space-charge-limited currents and trap-filled limit in one-dimensional insulators, *Journal of Physics D: Applied Physics* **17**, 135 (1984).

[18] C. Tanase, P. W. M. Blom, and D. M. de Leeuw, Origin of the enhanced space-charge-limited current in poly(*p*-phenylene vinylene), *Physical Review B* **70**, 193202 (2004).

[19] Q. Liao, Z. Qin, Z. Zhang, *et al.*, Investigation on the plasma-induced emission properties of large area carbon nanotube array cathodes with different morphologies, *Nanoscale Research Letters* **6**, 40 (2011).

[20] C. A. Spindt, I. Brodie, L. Humphrey, and E. R. Westerberg, Physical properties of thin-film field emission cathodes with molybdenum cones, *Journal of Applied Physics* **47**, 5248–5263 (1976).

[21] S. Sun and L. K. Ang, Onset of space charge limited current for field emission from a single sharp tip, *Physics of Plasmas* **19**, pages (2012).

[22] M. Hess and C. Chen, Space-charge limit for a finite-size bunched beam in a circular conducting pipe, *Physical Review Special Topics: Accelerators Beams* **7**, 092002 (2004).

[23] D. J. BenDaniel and C. B. Duke, Space-charge effects on electron tunneling, *Physical Review* **152**, 683–692 (1966).

[24] C. B. Wheeler, Space charge limited photoelectric emission in a plane parallel electrode geometry, *Journal of Physics A: General Physics* **5**, 1337 (1972).

[25] I. Langmuir, The effect of space charge and residual gases on thermionic currents in high vacuum, *Physical Review* **2**, 450–486 (1913).

[26] I. Langmuir, The effect of space charge and initial velocities on the potential distribution and thermionic current between parallel plane electrodes, *Physical Review* **21**, 419–435 (1923).

[27] G. Jaffé, On the currents carried by electrons of uniform initial velocity, *Physical Review* **65**, 91–98 (1944).

[28] R. R. Puri, D. Biswas, and R. Kumar, Generalization of the Child-Langmuir law for nonzero injection velocities in a planar diode, *Physics of Plasmas* **11**, 1178–1186 (2004).

[29] Y.-M. Quan and Y.-G. Ding, Generalization of the two-dimensional Child-Langmuir law for non-zero injection velocities in a planar diode, *Journal of Plasma Physics* **75**, 85–90 (2009).

[30] H. R. Jory and A. W. Trivelpiece, Exact relativistic solution for the one-dimensional diode, *Journal of Applied Physics* **40**, 3924–3926 (1969).

[31] M.-C. Lin and D. Chuu, Quasistationary states of a relativistic field-emission-limited diode employing a high-transparency mesh anode, *Applied Physics Letters* **80**, 4262–4264 (2002).

[32] Y. Feng and J. P. Verboncoeur, Consistent solution for space-charge-limited current in the relativistic regime for monoenergetic initial velocities, *Physics of Plasmas* **15**, 112101 (2008).

[33] Y. Y. Lau, D. Chernin, D. G. Colombant, and P.-T. Ho, Quantum extension of Child-Langmuir law, *Physical Review Letters* **66**, 1446–1449 (1991).

[34] L. K. Ang, T. J. T. Kwan, and Y. Y. Lau, New scaling of Child-Langmuir law in the quantum regime, *Physical Review Letters* **91**, 208303 (2003).

[35] L. K. Ang, W. S. Koh, Y. Y. Lau, and T. J. T. Kwan, Space-charge-limited flows in the quantum regime, *Physics of Plasmas* **13**, 056701 (2006).

[36] C. B. Wheeler, The neutralization of space charge in the planar diode: I. by the injection of positive ions, *Journal of Physics D: Applied Physics* **7**, 1336 (1974).

[37] M.-C. Lin, Space-charge effects of electrons and ions on the steady states of field-emission-limited diodes, *Journal of Vacuum Science Technology B: Microelectronics and Nanometer Structures* **23**, 636–639 (2005).

[38] C. Litwin and R. Rosner, Relativistic space-charge-limited bipolar flow, *Physical Review E* **58**, 1163–1164 (1998).

[39] C. B. Wheeler, The approach to space charge limited current flow between concentric spheres, *Journal of Physics A: Mathematical and General* **8**, 1159 (1975).

[40] L. Oksuz, Analytical solution of space charge limited current for spherical and cylindrical objects, *Applied Physics Letters* **88**, 181502 (2006).

[41] J. W. Luginsland, Y. Y. Lau, R. J. Umstattd, and J. J. Watrous, Beyond the Child–Langmuir law: a review of recent results on multidimensional space-charge-limited flow, *Physics of Plasmas* **9**, 2371–2376 (2002).

[42] J. J. Watrous, J. W. Luginsland, and M. H. Frese, Current and current density of a finite-width, space-charge-limited electron beam in two-dimensional, parallel-plate geometry, *Physics of Plasmas* **8**, 4202–4210 (2001).

[43] A. Rokhlenko and J. L. Lebowitz, Space charge limited flow of a thin electron beam confined by a strong magnetic field, *Physics of Plasmas* **11**, 4559–4563 (2004).

[44] B. Ragan-Kelley, J. P. Verboncoeur, and Y. Feng, Two-dimensional axisymmetric Child-Langmuir scaling law, *Physics of Plasmas* **16**, 103102 (2009).

[45] Y. Li, H. Wang, C. Liu, and J. Sun, Two-dimensional Child-Langmuir law of planar diode with finite-radius emitter, *Applied Surface Science* **251**, 19–23 (2005).

[46] A. Rokhlenko and J. L. Lebowitz, Space-charge-limited, two-dimensional unmagnetized flow in a wedge geometry, *Journal of Applied Physics* **102**, 123307 (2007).

[47] A. Rokhlenko, Space charge limited flow in a rectangular region: profile of the current density, *Journal of Applied Physics* **100**, 013305 (2006).

[48] R. J. Umstattd and J. W. Luginsland, Two-dimensional space-charge-limited emission: beam-edge characteristics and applications, *Physical Review Letters* **87**, 145002 (2001).

[49] J.-P. Girardeau-Montaut and C. Girardeau-Montaut, Space-charge-limited current density as a function of electron flow duration in an emissive diode, *Journal of Applied Physics* **65**, 2889–2895 (1989).

[50] M. E. Griswold, N. J. Fisch, and J. S. Wurtele, Amended conjecture on an upper bound to time-dependent space-charge limited current, *Physics of Plasmas* **19**, 024502–024504 (2012).

[51] C. K. Birdsall and W. B. Bridges, Space-charge instabilities in electron diodes and plasma converters, *Journal of Applied Physics* **32**, 2611–2618 (1961).

[52] E. A. Coutsias and D. J. Sullivan, Space-charge-limit instabilities in electron beams, *Physical Review A* **27**, 1535–1543 (1983).

[53] T. Westermann, A particle-in-cell method as a tool for diode simulations, *Nuclear Instruments and Methods in Physics Research Section A: Accelerators, Spectrometers, Detectors and Associated Equipment* **263**, 271–279 (1988).

[54] C. Birdsall, Particle-in-cell charged-particle simulations, plus monte carlo collisions with neutral atoms, pic-mcc, *IEEE Transactions on Plasma Science* **19**, 65–85 (1991).

[55] D. Beazley and P. Lomdahl, Feeding a large-scale physics application to Python, *Proceedings of the 6th International Python Conference* (1997).

[56] R. C. Davidson, *Physics of Nonneutral Plasmas* (Imperial College Press, 2001).

[57] J. J. Watrous, J. W. Lugisland, and G. E. Sasser III, An improved space-charge-limited emission algorithm for use in particle-in-cell codes, *Physics of Plasmas* **8**, 289–296 (2001).

[58] D. Biswas, R. Kumar, and R. R. Puri, Absence of saturation for finite injected currents in axially symmetric cavity diode, *Physics of Plasmas* **10**, 4521–4529 (2003).

[59] A. Sidi, Some properties of a generalization of the Richardson extrapolation process, *IMA Journal of Applied Mathematics* **24**, 327–346 (1979).

[60] Y. Feng and J. P. Verboncoeur, Transition from Fowler-Nordheim field emission to space charge limited current density, *Physics of Plasmas* **13**, 073105 (2006).

[61] M. C. Lin and J. P. Verboncoeur, Influence of ion effects on a space-charge-limited field-emission flow: from non-relativistic to ultra-relativistic regimes, Presented at the international vacuum electronics and vacuum electron sources conference (2012).

[62] J. P. Verboncoeur *et al.*, Object Oriented Particle-in-Cell 1-D (OOPD1), 2012, `http://ptsg.egr.msu.edu`.

[63] G. van Rossum *et al.*, The Python Language Reference, `http://python.org`.

[64] T. E. Oliphant, *Guide to numpy* (Provo, UT, 2006), `http://www.tramy.us/`.

[65] J. Hunter, Matplotlib: a 2D graphics environment, *Computing in Science & Engineering* **9**, 90–95 (2007).

[66] E. Jones, T. E. Oliphant, P. Peterson, *et al.*, SciPy: open source scientific tools for Python, 2001, `http://www.scipy.org/`.

[67] D. Shiffler, M. Haworth, K. Cartwright, *et al.*, Review of cold cathode research at the Air Force Research Laboratory, *IEEE Transactions on Plasma Science* **36**, 718–728 (2008).

[68] J. P. Verboncoeur, Symmetric spline weighting for charge and current density in particle simulation, *Journal of Computational Physics* **174**, 421–427 (2001).

[69] H. C. Kim, Y. Feng, and J. P. Verboncoeur, Algorithms for accurate collection, ejection, and loading in particle simulations, *Journal of Computational Physics* **223**, 629–642 (2007).